



**TÉCNICO**  
LISBOA

# **Estimating Sea Ice Thickness in the Arctic using ROV-based Underwater Hyperspectral Imaging**

**Lara Gemmrich**

Thesis to obtain the Master of Science Degree in

## **Electrical and Computer Engineering**

Supervisors: Prof. Alexandre José Malheiro Bernardino  
Prof. Martin Ludvigsen

### **Examination Committee**

Chairperson: Prof. João Manuel de Freitas Xavier

Advisor: Prof. Alexandre José Malheiro Bernardino

Members of the Committee: Prof. Knut Vilhelm Høyland

**November 2024**

## **DECLARATION**

I declare that this document is an original work of my own authorship and that it fulfills all the requirements of the Code of Conduct and Good Practices of the Universidade de Lisboa.

# Acknowledgments

Thank you to my supervisors, Alexandre Bernardino and Martin Ludvigsen. I also thank Knut Høyland for the opportunity to join his course on Sea Ice Mechanics and Physics on Svalbard, Norway, and for accommodating my fieldwork as part of this course. A large thank you to Leonard Günzel for leading the fieldwork, helping with the initial hyperspectral data processing, and for his feedback and comments on the thesis.

Finally, this thesis project would not have been possible without the funding of the Marine and Maritime Intelligent Robotics (MIR) Erasmus+ Programme, and my fellow MIR students. Thank you.

## Abstract

Sea ice thickness plays a crucial role in both the polar and global environment, influencing under-ice ecosystems, local and global weather patterns, ocean circulation, and climate change. It also significantly affects the safety and success of polar marine and maritime operations. Monitoring sea ice thickness is essential in understanding its impact on these interconnected systems.

Currently, ice thickness is largely measured using invasive, labour-intensive methods such as ice coring, or using under-ice multibeam sonars. Both of these methods present limitations and challenges.

This thesis introduces a novel approach to estimate sea ice thickness using Underwater Hyperspectral Imaging (UHI) measurements alongside physical ice and snow properties. Radiance data were collected under first year level ice using a Remotely Operated Vehicle (ROV) equipped with navigational sensors and an UHI camera during a field excursion in Van Mijenfjorden, Svalbard, in March 2024. The data were analysed to obtain spectral irradiance and spectral transmittance. Two radiative transfer models were applied to calculate spectral extinction coefficients and to estimate ice thickness for a variety of light scattering behaviours. The retrieved spectral extinction coefficients aligned with results from previous studies, and snow and ice thicknesses were successfully estimated. The closest agreement between the modelled and observed ice thickness was achieved when accounting for albedo influence, and assuming anisotropic scattering through bare ice and isotropic scattering through snow covered ice. These findings confirm that ROV-based light transmittance measurements from an UHI camera can successfully be used to retrieve sea ice thickness.

**Keywords:** sea ice thickness, Remotely Operated Vehicle (ROV), Underwater Hyperspectral Imaging (UHI), radiative transfer, light transmittance

## Resumo

A espessura do gelo marinho desempenha um papel crucial tanto no ambiente polar como global, influenciando ecossistemas sob o gelo, padrões meteorológicos locais e globais, a circulação oceânica e as alterações climáticas. Também afeta significativamente a segurança e o sucesso das operações marítimas polares. A monitorização da espessura do gelo é essencial para compreender o seu impacto nestes sistemas interligados.

Atualmente, a espessura do gelo é geralmente medida através de métodos invasivos e laboriosos, como a perfuração de gelo, ou com sonares multifeixe sob o gelo. Ambos os métodos apresentam limitações e desafios.

Esta tese apresenta uma nova abordagem para estimar a espessura do gelo marinho, utilizando medições de Imagem Hiperespectral Subaquática (UHI) juntamente com as propriedades físicas do gelo e da neve. Os dados de irradiância foram recolhidos sob gelo de primeiro ano, utilizando um Veículo Operado Remotamente (ROV) equipado com sensores de navegação e uma câmara UHI, durante uma excursão de campo em Van Mijenfjorden, Svalbard, em março de 2024. Os dados foram analisados para obter a irradiância e a transmitância espectral. Dois modelos de transferência radiativa foram aplicados para calcular os coeficientes de extinção espectral e estimar a espessura do gelo, considerando diferentes comportamentos de dispersão da luz.

Os coeficientes de extinção recuperados alinharam-se com estudos anteriores e as espessuras do gelo e da neve foram estimadas com sucesso. A melhor correspondência entre os resultados modelados e observados foi alcançada ao considerar a influência do albedo e a dispersão anisotrópica no gelo descoberto e isotrópica no gelo coberto de neve.

**Keywords:** espessura do gelo marinho, veículo operado remotamente (ROV), imagem hiperespectral subaquática (UHI), transferência radiativa, atenuação da luz



# Contents

<b>List of Tables</b>	<b>ix</b>
<b>List of Figures</b>	<b>xi</b>
<b>Glossary</b>	<b>xii</b>
<b>Acronyms</b>	<b>1</b>
<b>1 Introduction</b>	<b>2</b>
1.1 Motivation . . . . .	2
1.2 Project Description . . . . .	3
1.3 Aim and Objective . . . . .	4
1.4 Contributions . . . . .	5
<b>2 Theory and Background</b>	<b>6</b>
2.1 Physical Properties of Sea Ice . . . . .	6
2.2 Optical Properties of Sea Ice and Snow . . . . .	9
2.3 Ice and Snow Thickness Measurements . . . . .	11
2.4 ROVs for Underwater Operations . . . . .	12
2.5 Hyperspectral Imaging . . . . .	13
2.5.1 Ecotone UHI . . . . .	15
<b>3 Previous Works</b>	<b>16</b>
3.1 Under-ice Hyperspectral Imaging for Light Studies . . . . .	16
3.2 Other Under-Ice Light Field Studies . . . . .	19
3.3 Sea Ice Radiative Transfer Models . . . . .	20
3.4 Literature Gaps . . . . .	23

<b>4 Methodology</b>	<b>25</b>
4.1 Data Collection . . . . .	25
4.1.1 Double Blueye Robotic Platform . . . . .	26
4.1.2 Test Site Preparation . . . . .	28
4.1.3 Double Blueye Measurements . . . . .	29
4.2 Data Processing . . . . .	31
4.2.1 UHI Data Calibration . . . . .	31
4.2.2 Radiance and Irradiance Calculations . . . . .	33
4.2.3 Radiative Transfer Models . . . . .	38
<b>5 Results</b>	<b>40</b>
5.1 Radiative Transfer Models - Spectral Extinction Coefficients . . . . .	40
5.2 Estimating Ice Thickness Using Radiative Transfer Models . . . . .	41
5.3 Estimating Ice Thickness Using Stefan's Law . . . . .	50
5.4 Spectral Transmittance . . . . .	51
<b>6 Discussion</b>	<b>52</b>
6.1 Radiative Transfer Models - Spectral Extinction Coefficients . . . . .	52
6.2 Ice Thickness Estimation . . . . .	53
6.3 Spectral Transmittance Results . . . . .	55
6.4 Limitations . . . . .	56
<b>7 Conclusion</b>	<b>58</b>
<b>Bibliography</b>	<b>63</b>

# List of Tables

2.1	Technical specifications of the Scientific UHI-6 OV hyperspectral imager . . . . .	15
3.1	Summary of under-ice UHI light measurement studies. . . . .	17
3.2	Summary of snow, ice, and light transmittance observations from non-UHI studies. . . . .	19
4.1	Above-ice measurement timestamps. . . . .	29
4.2	Overview of successful DBE flights. . . . .	30
4.3	Snow Depth measurements along the ROV transect. . . . .	31
4.4	Ice and snow thickness measurements in surrounding area. . . . .	31
4.5	Anisotropic scattering coefficients. . . . .	37
4.6	Comparison of mean total irradiance measurements. . . . .	38
5.1	Stefan's Law parameters with their corresponding units. . . . .	50
5.2	Total transmittance and standard deviation through bare and snow-covered ice. . . . .	51
6.1	Comparison of modelled ice and snow thickness with measured data assuming same scattering through snow and ice . . . . .	54
6.2	Comparison of modelled ice and snow thickness with measured data assuming isotropic scattering through snow-covered ice and anisotropic scattering through bare ice . . . . .	54

# List of Figures

1.1	Location of field excursion in Van Mijenfjorden, Svalbard, Norway . . . . .	4
2.1	Schematic of sea ice structure . . . . .	7
2.2	Basal planes and c-axis structure of sea ice . . . . .	8
2.3	Visible part of electromagnetic spectrum . . . . .	9
2.4	Blueye Pro ROV . . . . .	12
2.5	Optical signature of an alga displayed in RGB, and as a contiguous spectrum . . . . .	13
2.6	Four predominant hyperspectral scanning methods . . . . .	14
2.7	Setup of a PGP imaging spectrograph . . . . .	14
3.1	Light transmittance measurements from the MOSAiC project . . . . .	18
3.2	Under-ice downwelling radiance measurements . . . . .	18
3.3	Spectral transmittance for selected cases . . . . .	20
3.4	Spectral extinction coefficients calculated for various snow and ice conditions . . . . .	21
3.5	Relative downwelling irradiance and spectral irradiance extinction coefficients . . . . .	23
4.1	Initial field test on Svalbard in Longyearbyen. Air temperature $-20^{\circ}\text{C}$ . . . . .	25
4.2	Packaging of the DBE for the snow scooter sledge . . . . .	25
4.3	Schematic representation of the DBE system setup . . . . .	26
4.4	Networking setup of the DBE platform . . . . .	27
4.5	ROV piloting station . . . . .	27
4.6	Svea test site . . . . .	28
4.7	DBE launch and under-ice operation . . . . .	28
4.8	Using the UHI to take reflected radiance measurements . . . . .	29
4.9	Cleared runway for DBE to follow . . . . .	29

4.10 Plot of DVL track from run 6 . . . . .	30
4.11 UHI data image renderings . . . . .	33
4.12 Spectral radiance measurements used to validate the data . . . . .	34
4.13 Mean incoming and transmitted spectral radiance plots for flights 4 and 6 . . . . .	36
4.14 Normalized under-ice spectral radiance for flights 4 and 6 . . . . .	36
4.15 Incoming and transmitted spectral irradiance for flights 4 and 6 . . . . .	37
5.1 Spectral extinction coefficients calculated for snow and bare ice . . . . .	41
5.2 Optimized snow depth and ice thickness estimations from flight 4 data using the Perovich model . . . . .	42
5.3 Optimized snow depth and ice thickness estimations from flight 4 data using the Nicolaus and Katlein model . . . . .	43
5.4 Optimized snow depth and ice thickness estimations from flight 6 data using the Perovich model . . . . .	44
5.5 Optimized snow and ice thickness from flight 6 data using the Nicolaus and Katlein model	45
5.6 Optimized snow depth and ice thickness estimations from flight 4 data using the Perovich model assuming isotropic scattering for snow-covered ice and anisotropic scattering for bare ice . . . . .	46
5.7 Optimized snow depth and ice thickness estimations from flight 4 data using the Nicolaus and Katlein model assuming isotropic scattering for snow-covered ice and anisotropic scattering for bare ice . . . . .	47
5.8 Optimized snow depth and ice thickness estimations from flight 6 data using the Perovich model assuming isotropic scattering for snow-covered ice and anisotropic scattering for bare ice . . . . .	48
5.9 Optimized snow depth and ice thickness estimations from flight 6 data using the Nicolaus and Katlein model assuming isotropic scattering for snow-covered ice and anisotropic scattering for bare ice . . . . .	49
5.10 Freezing degree days at Akseløya Weather Station . . . . .	50
5.11 Spectral transmittance calculated for bare ice and snow-covered ice for flights 4 and 6 . .	51
6.1 Best results of optimized snow depth and ice thickness estimations . . . . .	55

# Glossary

$C$  Radiance to irradiance conversion factor.  $C = 2.5 - 2\gamma$ . 22, 36–38, 40, 51, 53, 55, 56

$E$  Irradiance, measured in  $Wm^{-2}$ . 10

$E(\lambda)$  Spectral irradiance, measured in  $Wm^{-2}nm^{-1}$ . 9, 11, 22

$L(\lambda)$  Spectral radiance, measured in  $Wm^{-2}sr^{-1}nm^{-1}$ . 9, 22, 32

$R(\lambda)$  Spectral reflectance. 10

$\alpha_T$  Total albedo. 10

$\alpha_\lambda$  Spectral albedo. 10, 21, 22, 39

$\gamma$  Anisotropic scattering coefficient. 22

$\kappa_\lambda$  Spectral extinction coefficient. 11, 21

$\lambda$  Wavelength. 9, 13, 32, 33

# Acronyms

**AUV** Autonomous Underwater Vehicle. 11, 12

**DBE** Double Blueeye. ix, 25–30, 35, 57, 58

**DN** Digital Number. 32

**DVL** Doppler Velocity Log. 3, 26, 27, 30

**ESM** Earth System Model. 19

**FDD** Freezing Degree Days. 7, 50

**MOSAiC** Multidisciplinary drifting Observatory for the Study of Arctic Climate. 16, 18, 56

**MRE** Mean Relative Error. 41

**OOI** Object of Interest. 13

**PAR** Photosynthetically Active Radiation. 16, 17

**PGP** Prism-Grating-Prism. 14

**ROV** Remotely Operated Vehicle. iii, 3, 6, 11, 12, 15, 16, 26–28, 30, 33, 57

**SAR** Synthetic Aperture Radar. 12

**SBE** Single Blueeye. 27, 30

**TARTES** Two-streAm Radiative TransfEr in Snow. 38, 39

**UHI** Underwater Hyperspectral Imaging. iii, xi, 5, 6, 13, 15–17, 23, 24, 26, 27, 29, 31–33, 35, 57–59

**UNIS** University Centre in Svalbard. 3, 6, 28

# Chapter 1

## Introduction

The Arctic environment has gained increasing attention in recent years, positioning Arctic research at the forefront of scientific inquiry, particularly in areas related to climate change and marine ecosystems. Sea ice, specifically, plays a crucial role in ocean circulation, weather patterns, and temperature regulation [1]. Understanding sea ice cover and thickness is fundamental for the survival of northern communities, and the knowledge can enhance our comprehension of the intricate interactions between the Arctic region and the global climate system.

The primary objective of this thesis is to retrieve under-ice light measurements at a field location on Svalbard, Norway and use these data to estimate sea ice thickness. By analysing spectral attenuation through ice and snow and comparing it with physical and optical properties, the aim is to establish a relationship between ice thickness and the amount of light penetrating the ice.

This approach offers a non-invasive method for large-scale coverage and temporal monitoring. Underwater hyperspectral imaging can be conducted repeatedly over time to monitor changes in ice thickness. These insights into seasonal and long-term sea ice dynamics can refine climate models and contribute to a better understanding of Arctic ecosystems, both crucial for the protection of polar environments.

### 1.1 Motivation

Sea ice covers more than 7% of the Earth's surface, either seasonally or permanently [2]. The motivation for studying sea ice thickness is multifaceted, encompassing environmental concerns [3], Arctic transportation [4], and polar operations and engineering [5, 6]. Sea ice impacts local ecosystems, ocean and atmospheric heat exchange, ocean circulation, and global climate patterns, all of which are influenced by the amount of light that is reflected, absorbed, or transmitted through the ice.

Over the last decade, Arctic sea ice has been declining, becoming thinner and more seasonal, leading to increased light absorption by the ocean and altering the surface energy budget of the Arctic Ocean [7]. Long-term monitoring of the changing sea ice thickness can offer valuable insights into sea ice melting rate, which is a critical indicator of climate change.

Ice thickness also directly affects the amount of light that penetrates the ice, which significantly influences under-ice primary productivity [8], sea-ice mass balance, and geochemical processes [7]. The shift from thick, multi-year ice to seasonal, thinner ice has also sparked greater interest in Arctic shipping

[4]. However, sea ice poses a significant risk to polar maritime operations. Accurate ice thickness data enhances safety and efficiency in operations such as load assessments for icebreakers and offshore structures [5].

Despite its critical importance, sea ice thickness is currently one of the most inaccurately measured sea ice parameters [5]. To address this gap, we propose a method of estimating sea ice thickness using under-ice light field measurements.

Traditional methods of measuring ice thickness, such as ice-coring, are invasive, time-consuming, labour-intensive, and limited in spatial coverage. Ice coring requires thick ice to support the weight of personnel, meaning this method is not valid for measuring very thin ice ( $<0.3\text{m}$ ). It also involves physically demanding work in harsh and remote environments, posing significant risks.

In contrast, measuring light transmittance under the ice is non-invasive and avoids physical disturbance, allowing for repeated measurements of the same area. Measurements can be taken remotely, using underwater vehicles or buoys. This enables spatial and temporal measurements as well as studies of seasonal and long-term dynamics, and significantly improves operator safety.

Multibeam sonars are another common sensor used to measure ice thickness [9, 10]. While they are non-intrusive, sonars measure only the ice draft (*i.e.* the portion of the ice below the waterline). Additionally, these instruments do not account for snow cover. Ice and snow both have distinct optical properties influencing the amount of light that can pass through, so by establishing a relationship between the snow and ice layers and the light transmittance, we can derive more comprehensive estimates of overall ice thickness and snow depth.

In summary, using under-ice light transmittance data to estimate ice thickness is non-invasive, efficient, and scalable. It holds the potential for long-term and remote monitoring, and is relevant for understanding ice-related processes in the context of climate change and ecological health.

## 1.2 Project Description

For this thesis project, we collected incoming and under-ice radiance data over a four-day field excursion to Van Mijenfjorden, Svalbard in March 2024. Data were gathered using an underwater robotic platform comprising two Remotely Operated Vehicle (ROV)s, and equipped with an altimeter, a Doppler Velocity Log (DVL), a light source, and a hyperspectral camera. The fieldwork location is marked in Figure 1.1, and was conducted in collaboration with the Arctic Technology course on Sea Ice Mechanics and Physics (AT-311) at the University Centre in Svalbard (UNIS). While our group focused on collecting the under-ice data, other student groups measured the physical properties of snow and ice.

To analyse the data, we converted radiance measurements to irradiance, and applied two radiative transfer models to obtain the spectral extinction coefficients of the ice and snow. These models also incorporated the physical parameters measured during the field expedition. Using these results, we estimated sea ice thickness and snow depth. The results were validated with the ground truth data of ice thickness and snow depth. This method provides a novel, non-invasive approach to sea ice monitoring, with significant implications for Arctic research and climate studies.



Figure 1.1: Data for this thesis project were collected at the Svea field station (marked F on this chart) located in Van Mijenfjorden on Svalbard, Norway.

### 1.3 Aim and Objective

While sea ice optics have been extensively studied (e.g. [11, 12, 13, 14]), knowledge of radiative transfer and absorption in sea ice remains limited due to the challenges of accessing the under-ice environment and acquiring reliable *in situ* measurements [15]. Many under-ice light studies lack coincident snow depth and ice thickness measurements, making it difficult to investigate direct relationships [16]. While ice thickness measurements have been used to infer light attenuation [17], the reverse - inferring ice thickness from light attenuation - remains largely unexplored.

In this project we investigate the relationship between ice thickness, snow depth, and light transmittance. We aim to develop a novel ice-thickness measurement method, with the following research question guiding this study.

*Can incoming and under-ice light measurements be used to infer sea ice thickness and snow depth, and how does this method compare to conventional ice-thickness measurement techniques?*

The main objectives of this thesis are to:

- Measure incoming and under-ice light transmittance using hyperspectral radiance data during a field campaign on Svalbard.

- Convert radiance data to irradiance and apply radiative transfer models to estimate spectral extinction coefficients for ice and snow.
- Calculate spectral and total transmittance through bare and snow-covered ice.
- Develop and validate a method to infer sea ice thickness and snow depth from light transmittance data and physical snow properties.

## 1.4 Contributions

Inferring ice thickness from light attenuation has not been fully explored, despite the established theoretical basis for light propagation in sea ice. Our approach addresses this gap, leveraging advancements in hyperspectral imaging techniques, and employing remotely operated underwater platforms. Validating the method in-field provides a proof-of-concept that can be expanded upon in future studies and used in ongoing Arctic monitoring programs. Few studies have collected coincident optical and physical measurements of ice and snow.

The main contributions of this project are outlined below:

- We present a novel application of using UHI data to infer sea ice thickness and snow depth, filling a gap in current sea ice monitoring techniques.
- Through the integration of radiative transfer modelling with field-based measurements, we link the physical and optical properties of ice and snow, providing a more complete understanding of light transmission through ice.
- We validate the proposed sea ice monitoring technique in-field, collecting coincident optical and physical measurements of ice and snow.

The method presented in this research can be applied to remote or autonomous platforms, minimizing human impact on the fragile polar ecosystems. Additionally, it can complement existing ice thickness measurement techniques, such as ice coring, multibeam sonar, or satellite-based methods.

The theoretical background needed for this project is outlined in Chapter 2. Chapter 3 reviews state-of-the-art studies involving underwater hyperspectral imaging and under-ice light transmittance, and identifies gaps in the current literature. In Chapter 4 we outline the data collection and data analysis methods. The results are presented in Chapter 5 and discussed in Chapter 6. Final conclusions and suggestions for future work can be found in Chapter 7.

## Chapter 2

# Theory and Background

For the successful creation and analysis of the sea ice thickness model, some background knowledge on sea ice structure and mechanics, as well as the optics of sea ice and snow, is necessary. We give a brief introduction to current ice thickness measurement techniques, and to ROVs used for underwater light measurements. Finally, we introduce underwater hyperspectral imaging, and the specific UHI used for this project.

The information presented in Section 2.1 is taken from the University Centre in Svalbard (UNIS) *AT-344 Arctic Marine Measurements Techniques, Operations and Transport* and *AT-311 Sea Ice Physics and Mechanics* course compendium [18].

### 2.1 Physical Properties of Sea Ice

Pertaining to physical properties of ice, sea ice thickness is of particular interest. Ice thickness depends on meteorological conditions (air temperatures, radiation, precipitation, and wind), oceanic conditions (velocity, salinity, and temperature) and physical constraints such as islands or land [19].

Sea ice is a highly spatially complex material, both horizontally and vertically, and the surface of sea ice can differ largely, especially over a large area. The ice surface can be bare, covered by fresh, smooth snow, covered by disturbed snow, or covered in melt ponds. For our studies, we deal only with bare and snow-covered first year level ice, *i.e.* ice that has a flat surface and has not been deformed in any way.

On a macro scale, sea ice can be classified as having three main vertical components, which are defined depending on their relative position to the sea surface. An ice slab is composed of sea ice draft  $h_d$  and sea ice freeboard  $h_f$ . If snow is present, another layer  $h_s$  on top of the ice is introduced. A schematic representation of sea ice vertical components is shown in Figure 2.1.

The ice draft refers to the partial sea ice thickness measured from the bottom of the ice up to the sea surface, and freeboard is defined as the distance from the waterline up to the top of the ice. The total sea ice thickness  $h_i$  is found by summing the values of  $h_d$  and  $h_f$ .

Ice thickness in the Arctic basin generally ranges from around  $2\text{ m}$  in the summer to  $3\text{ m}$  in the winter [20]. A simple way to estimate variations in level ice thickness is by using Stefan's Law ([18]). The law relates the change in ice thickness over a given amount of time to the physical ice properties and the

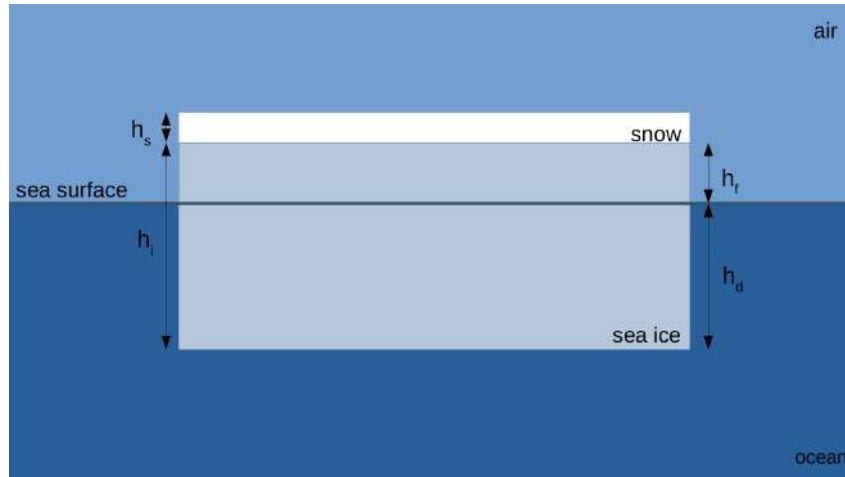


Figure 2.1: Schematic of sea ice structure.

temperature. The model can be applied using air temperatures and making the following assumptions:

- No snow
- No heat transfer from the ocean to the ice; that is  $q_{ocean} = 0$ .
- No solar radiation
- Linear temperature profile through the ice sheet
- Fourier's law;  $q_i = -k\Delta T/\Delta z$
- $q_{lat} = q_i = q_{sur}$
- Surface water temperature is equal to freezing point

Here,  $q_{ocean}$ ,  $q_{lat}$ ,  $q_i$ , and  $q_{sur}$  represent the heat transfers from the ocean to the ice ( $q_{ocean}$ ), from the newly forming ice at the bottom of the ice sheet to the already existing ice ( $q_{lat}$ ), from the ice to the air ( $q_i$ ), and within the air above the ice ( $q_{sur}$ ). The parameter  $k$  is the thermal conductivity,  $\Delta T$  is the change in temperature within the ice, and  $\Delta z$  is the change in depth.

A final assumption is that all energy released when the new ice layer forms is transported through the ice and out into the air. This is called flux and can be expressed through Fourier's law. With all the assumptions, Stefan's law [18] can be expressed as:

$$h_i^2(t) - h_{i,0}^2 = \frac{2k_i}{\rho_i l_i} FDD\alpha, \quad (2.1)$$

where  $h_i$  and  $h_{i,0}$  are the current and initial ice thickness, respectively. The left hand side of the equation calculates the change in ice thickness from the starting time to a given time. On the right hand side,  $k_i$  is the thermal conductivity,  $\rho_i$  the density, and  $l_i$  the latent heat of the ice. Freezing Degree Days (FDD) quantifies the amount of energy that has passed through the surface, and it comes from the assumption that air temperature is constant. It indicates the cumulative cooling effect over time, and accounts for the required energy for the ice to freeze. It can be seen then, that ice growth and formation are controlled by parameters that are affected by temperature fluctuations and varying daylight duration. Seasonal trends

thus play a large role in ice formations, as there is a major difference between the parameters in the winter and summer in the Arctic.

The scaling factor  $\alpha = 86400$  seconds/day.

Stefan's law is a simple way to calculate the variations in ice thickness with limited information, but the law can be refined to take into consideration the effect of snow, and the air boundary layer. While the original law assumes no snow is present on the ice, this is not the case with our data. Accounting for a layer of snow, the following can be derived from (2.1):

$$h_i^2(t) - h_{i,0}^2 + \frac{2h_s k_i}{k_s} h_i(t) - \frac{2h_s k_i}{k_s} h_{i,0} = \frac{2k_i}{\rho_i l_i} F D D \alpha \quad (2.2)$$

where the parameters  $h_s$  (snow depth) and  $k_s$  (thermal conductivity of snow) are introduced [18]. The two new terms,  $\frac{2h_s k_i}{k_s} h_i(t)$  and  $\frac{2h_s k_i}{k_s} h_{i,0}$ , account for impact of the snow insulation on ice growth. The snow layer increases the effective thickness through which heat must be conducted, which is influenced by the thermal conductivity of both snow ( $k_s$ ) and ice ( $k_i$ ).

To better understand the vertical complexity of sea ice and the effects it has on the optical properties of the ice, we need to examine the structure of sea ice at a closer level.

Sea ice consists of an intricate lattice structure of ice crystals. Due to the specific arrangement of hydrogen and oxygen atoms, parallel planes with different densities form, as illustrated in Figure 2.2. The denser planes, known as basal planes, are oriented perpendicular to the vertical optical axis of the ice, called the c-axis.

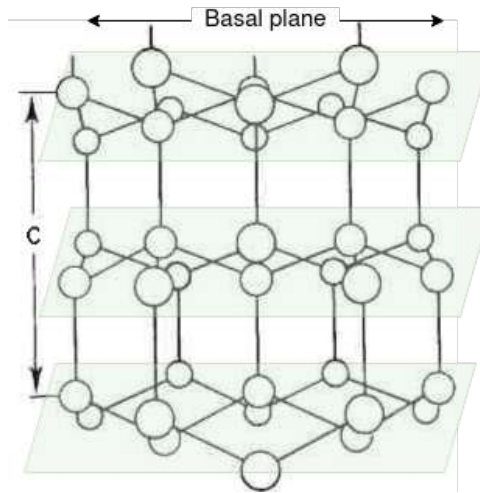


Figure 2.2: Basal planes and c-axis structure of sea ice [21].

Sea ice forms close to its melting point, meaning that liquid brine pockets remain between the ice crystals even when temperatures are below zero degrees Celsius. During the initial stages of the sea ice formation process, crystals grow in random orientations. As the ice continues to grow, particles grow more quickly along the basal plane, as this requires less energy. During phases of growth, sea water with higher salinity is expelled, and solid salt crystals are trapped, since they cannot be embedded in the crystal lattice. This process leads to the formation of brine pockets that stay fluid, even as the surrounding ice solidifies.

The different crystal orientations can be determined by their distinct optical properties. Light passing

through the optical axis of a crystal is undisturbed, while it is refracted in other directions. Shining a uni-polar light at a thin slice of ice highlights the different ice crystals as the light is scattered in different directions, making the crystals appear as different colours. This crystal structure and the brine volume also has a large effect on the scattering of light through sea ice. This leads us to the optical properties of sea ice and snow.

## 2.2 Optical Properties of Sea Ice and Snow

Optical properties are the parameters needed to describe concepts such as reflection, absorption, and transmission of solar radiation by sea ice [11]. While these properties extend from ultraviolet light (250-400  $nm$ ), through visible light (400-700  $nm$ ), to near-infrared light (750-2500  $nm$ ), we focus only on the visible spectrum for this work. Visible wavelengths and their corresponding colours can be seen in Figure 2.3.

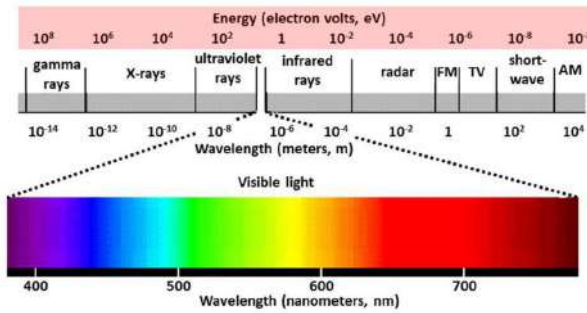


Figure 2.3: Visible part of electromagnetic spectrum

To understand the optics of sea ice, it is first necessary to learn some definitions:

**Spectral radiance**, denoted by  $L(\lambda)$  where  $\lambda$  is the wavelength, is the amount of light that is emitted, reflected, transmitted, or received by a surface (Watts) per unit projected area ( $m^2$ ) per unit solid angle ( $sr$ ) per wavelength ( $nm$ ). The SI units for spectral radiance are  $W m^{-2} sr^{-1} nm^{-1}$ . Spectral radiance is often also denoted as either downwelling ( $L_d(\lambda)$ ) or upwelling ( $L_u(\lambda)$ ) spectral radiance, where downwelling refers to the light that is emitted from, or transmitted through, a light source, and upwelling is used to denote the light received by or reflected off a surface.

**Spectral irradiance** is the spectral radiance projected onto a plane and integrated over a hemisphere. This results in a scaling by  $\cos\theta$ . We denote it by  $E(\lambda)$ , but  $F(\lambda)$  is also a frequently used notation (e.g. [11, 22]). Downwelling spectral irradiance  $E_d(\lambda)$  refers to the spectral radiance integrated over downward directions, and upwelling spectral irradiance  $E_u(\lambda)$  refers to the spectral radiance integrated over upward directions. Formally, downwelling spectral irradiance can be expressed by the following equation, adapted from [11]:

$$E_d(\lambda) = \int_{\phi=0}^{2\pi} \int_{\theta=0}^{\pi/2} L(\lambda) \cos\theta \sin\theta d\theta d\phi \quad (2.3)$$

where  $\theta$  is the zenith angle,  $\phi$  is the azimuth angle, and  $\lambda$  is the wavelength. Upwelling spectral irradiance is measured similarly, with the inner integration changed to be between  $\pi/2$  and  $\pi$ . Spectral irradiance is measured in  $W m^{-2} nm^{-1}$ .

For an isotropic radiance distribution, both downwelling and upwelling spectral irradiance simplify to:

$$E(\lambda) = \pi L(\lambda) \quad (2.4)$$

**Irradiance**, denoted as  $E$ , is the spectral radiance integrated over wavelengths and the solid angle, and is measured in  $Wm^{-2}$ . Irradiance describes the light intensity.

**Reflectance** describes the amount of light that is reflected off the surface of an object. It is the ratio of reflected radiant energy to incident radiant energy, and therefore a relative and dimensionless unit. Reflectance can be either spectral or diffuse. **Spectral reflectance**,  $R(\lambda)$ , is typical of smooth surfaces such as bare sea ice, and can be expressed as follows:

$$R(\lambda) = \frac{L_u(\lambda)}{L_d(\lambda)} \quad (2.5)$$

**Diffuse reflectance** scatters light in every direction, resulting in a more uniform reflection. This diffuse reflection is stronger at sunset, as the light has a farther path to travel through the atmosphere. Snow also scatters light in a diffuse manner due to its crystalline macro-structure.

**Spectral albedo**, denoted  $\alpha_\lambda$ , is defined as the fraction of the incident irradiance that is reflected [11]. The **total albedo**,  $\alpha_T$ , is the spectral albedo integrated over all wavelengths. It is a measure of the total solar energy absorbed by a surface [20], in our case snow and ice. Total albedo depends on the spectral distributions of the incoming light and reflected light, and so the albedo of a surface can change with the weather conditions, especially cloud cover. For example, on a clear day, the albedo of ice and snow will be higher than on a cloudy day. Albedo values will also change throughout the day, with varying sun angles. Albedo takes on values between 0 (if no light is reflected) and 1 (if all light is reflected).

**Spectral transmittance** is the amount of light that remains after travelling through an optical path, such as snow or sea ice. Mathematically, it is the ratio between the incident irradiance and the irradiance transmitted through the ice, and can be calculated as follows:

$$T(\lambda) = \frac{E_T(\lambda)}{E_S(\lambda)} \quad (2.6)$$

where  $E_T(\lambda)$  is the transmitted spectral irradiance, and  $E_S(\lambda)$  is the incident spectral irradiance. Transmittance is largely influenced by surface conditions, snow depth, and ice thickness, with snow depth having the largest impact. Transmittance decreases roughly exponentially as the ice thickness increases or snow gets deeper [22].

Optical properties of sea ice vary greatly, both spatially and temporally. In order to interpret observations and understand transmittance of light through sea ice, **radiative transfer models** are essential, as they simulate how sunlight interacts with the ice and snow cover.

The simplest and most commonly used sea ice radiative transfer model is the exponential decay relationship given by (2.7), adapted from [11]. This law is a variation of the Bouguer-Lambert law, or Beer's law, with the addition of the spectral albedo  $\alpha_\lambda$  term. The model assumes irradiance decreases exponentially through a homogeneous material of infinite optical thickness.

$$E(\lambda, z) = (1 - \alpha_\lambda)E_0(\lambda)e^{-\kappa_\lambda z} \quad (2.7)$$

Here,  $\kappa_\lambda$  is the **spectral extinction coefficient**,  $E(\lambda, z)$  is the transmitted spectral irradiance at depth  $z$ , and  $E_0(\lambda)$  is the incoming spectral irradiance. Since we are only concerned with transmitted irradiance under the ice and not within the ice, we use  $E(\lambda)$  to represent  $E(\lambda, z)$  where  $z$  is equal to the ice thickness.

The extinction coefficient measures the energy loss due to scattering and absorption, and classifies light attenuation in ice and snow [11]. It is commonly used to monitor primary productivity, ecosystems, and biogeochemical cycles under the ice [23, 24].

## 2.3 Ice and Snow Thickness Measurements

Sea ice research is a quickly expanding field, with much focus on sea ice thickness. Ice thickness can generally be measured from above or below the ice using sensors, or through direct measurements on the ice. Underneath the ice, sensors are commonly mounted on ROVs or AUVs. Above the ice, measurements can be taken from airborne laser scanners and cameras on drones or helicopters, or from satellite images such as ICESat-2 [25]. These sensors are most commonly acoustic or electromagnetic. Direct measurements usually involve drilling holes in the ice and measuring the ice thickness directly.

Spectroradiometers are sensors that can be used both above and below ice. They rely on the distinct electromagnetic properties of ice at various frequencies. For ice thickness measurements, microwave range frequencies are typically chosen, as ice has distinct absorption and emission characteristics at these frequencies. The microwaves can penetrate the ice to a certain depth, depending on the frequency. As a result, the strength of the signal received by radiometer is directly correlated to the depth of the ice. The received signals are processed to extract this information. The accuracy of ice thickness measurements using spectroradiometers can be affected by factors such as the presence of water on the ice (melt ponds) and snow cover.

Hyperspectral imagers are not currently used for direct ice thickness measurements, but they can provide information about the ice properties and composition [8, 16, 26], which can indirectly contribute to understanding ice thickness. They provide a large number of spectral bands across the electromagnetic spectrum. Taking the mean of these spectral bands allows the data to be processed in a similar way to the spectroradiometer data.

Electromagnetic sensors can also be used to measure ice thickness [1]. These sensors operate on electromagnetic induction principles, emitting a time-varying electromagnetic field into the ice. These induced fields generate secondary electromagnetic fields that are detected by the sensor and provide information about the electrical conductivity and depth of the ice. Electromagnetic sensors are typically mounted on a sled so that measurements can be taken at regular intervals along transects across the required region. The sensor records the secondary electromagnetic fields generated by the ice. In order to obtain relevant information from these data, they need to be inverted. This is done with inversion algorithms using a geophysical software such as EM Flow (Informer Technologies, LA, USA), which provides tools for 1D, 2D, and 3D inversion and interpretation in the time and frequency domains. The electromagnetic responses are correlated with the electrical properties of the materials, and the inversion results provide an estimation of the depth to the subsurface interfaces, including the bottom of

the ice.

Satellite-based Synthetic Aperture Radar (SAR) images can measure the height of the sea ice surface above the sea level to obtain satellite altimetry. By comparing satellite altimetry measurements before and after the formation of sea ice, ice thickness can be estimated. However, this method is more effective for large areas and thicker ice due to its large spatial footprint and lower resolution. As a result, satellite data were not used for this project.

Ice thickness can also be measured directly by drilling holes in the ice to extract ice cores. This method is highly labour intensive, but extremely effective - the length of the core provides an accurate thickness measurement of the ice in that location.

## 2.4 ROVs for Underwater Operations

Underwater vehicles open up a whole new world of research, allowing for measurements in the sea that would be difficult to reach otherwise. Autonomous Underwater Vehicle (AUV)s and Remotely Operated Vehicle (ROV)s are especially appealing for these types of tasks. Recently, the use of underwater robots to explore the waters beneath ice cover has increased [27]. These robots can be deployed through a single hole, enabling them to navigate a broader area without the need for multiple penetrations of the ice.

However, under-ice operations are difficult and risky, especially near the magnetic poles, where autonomous navigation can be challenging [28]. The risk of losing a vehicle is increased by the ice cover, as the robot cannot surface easily if communication is lost, unlike in open waters. For these reasons, AUVs were not considered for this mission. Small ROVs present an appealing alternative, since they are straightforward to use, and do not face these navigational challenges.

For our experiments we used two Blueye Pro (Trondheim, Norway) ROVs (Figure 2.4). The Blueye Pro model is an easy to use, professional ROV, with the option to automate depth and heading control. The ROV is able to dive to depths of 305 *m*, and can move forward at up to 5.6 *km/h* (3 *kts*), battling up to 3.7 *km/h* (2 *kts*) of current. The robot is also equipped with a tiltable full HD camera, which can be used for navigation and to record the dive. The range of the ROV depends on the length of the tether - in our case, we had a tether of 300 *m*.



Figure 2.4: Blueye Pro ROV (Trondheim, Norway).  
Dimensions: 485 x 257 x 354 *mm* (LxWxH).

## 2.5 Hyperspectral Imaging

Hyperspectral imaging involves capturing and processing information from across the electromagnetic spectrum, and provides a detailed spectral profile for each pixel in an image. As opposed to standard RGB cameras, which capture three wavebands of visible light (red, green, blue), hyperspectral imagers can capture light at  $<1\text{ nm}$  intervals, yielding over 300 values within the visible light range [29]. The Underwater Hyperspectral Imaging (UHI) used in this study captures 209 wavebands ranging from 380-750  $\text{nm}$  with a spectral resolution of approximately 1.88  $\text{nm}$ .

Figure 2.5 [29] shows the optical signature of a type of alga displayed in RGB and as a contiguous spectrum, clearly highlighting the difference in the amount of detail available from a standard digital camera versus a hyperspectral camera.

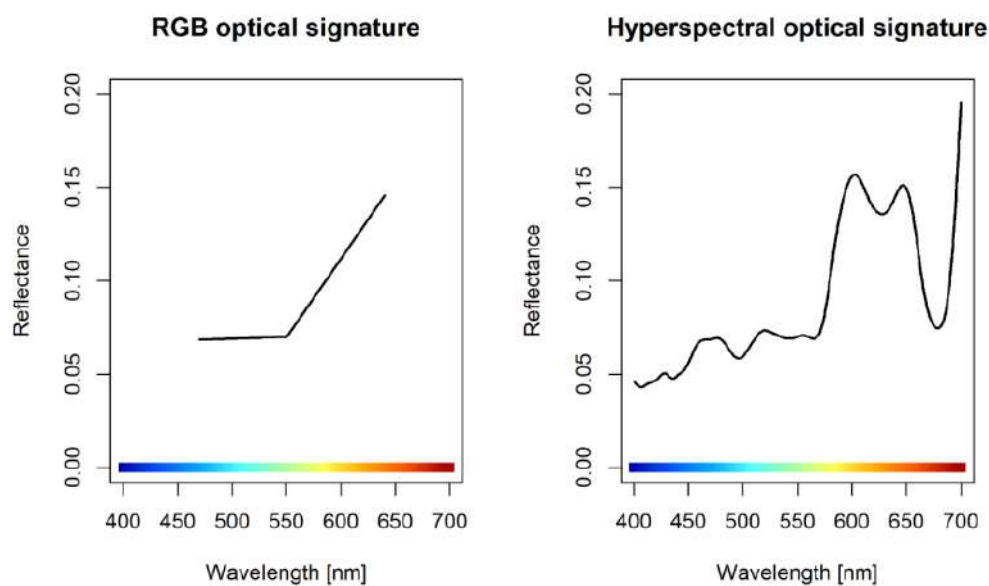


Figure 2.5: The optical signature of an alga displayed in RGB, and as a contiguous spectrum. The left image represents the information given by a regular digital camera, while the right shows the equivalent information that would be received by a UHI camera. Image taken from [29].

The image captured by a UHI can be thought of as a three dimensional data cube with two spatial dimensions  $x$  and  $y$ , and one spectral dimension  $\lambda$ . The most common hyperspectral image acquisition techniques are the *point-scanning* or *whisk-broom* method, and the *line-scanning* or *push-broom* method, shown in Figure 2.6a and 2.6b, respectively.

The UHI used for this work uses the push-broom method to capture detailed optical signatures of underwater environments and Object of Interest (OOI)s. Each UHI pixel is assigned its own contiguous light spectrum, which provides a high spectral resolution, and maintains detailed spatial information along the one spatial dimension [29].

In point-scanning, a single point is scanned at a time. In order to capture the entire image, the sensor or OOI needs to be moved along the two spatial dimensions. In line-scanning, the sensor measures all hyperspectral pixels along one spatial dimension simultaneously by capturing light entering the instrument through a thin slit. To capture image transects, the sensor is then moved across the target area, with the slit oriented perpendicularly to the direction of movement. The sensor continuously captures these lines of pixels at a set frame rate. These frames are then merged together to form a photomosaic image.

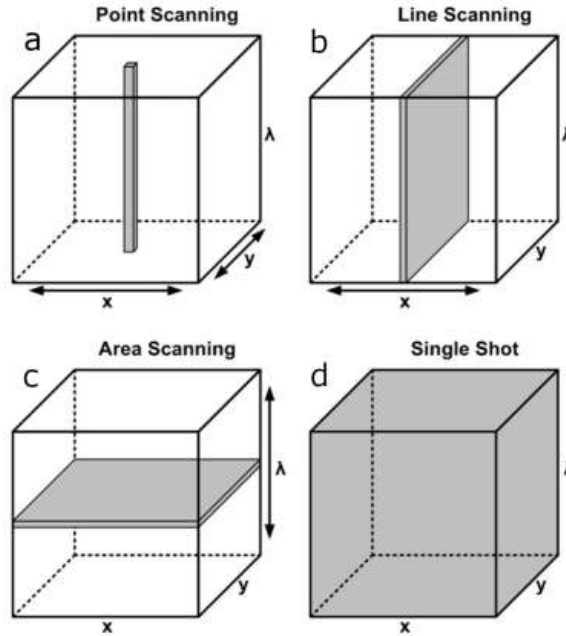


Figure 2.6: The four predominant hyperspectral scanning methods (a) Point-Scanning, (b) Line-Scanning, (c) Area-Scanning and (d) Single Shot visualized using a data cube. Figure taken from [30]

Both of these methods capture the entire spectral dimension at once. In order to discriminate between the different wavebands, a dispersion device is integrated into the camera. The hyperspectral camera used in this work includes an imaging spectrograph with transmission gratings, as shown in Figure 2.7. The light passes through the entrance slit, being received in one spatial dimension. The front lens of the spectrograph collimates the light beam, after which it is diffracted into separate wavelengths by the Prism-Grating-Prism (PGP) component, and projected through the back lens onto the detector (*i.e.* camera sensor). The spectral information is acquired by the detector row by row along the vertical axis.

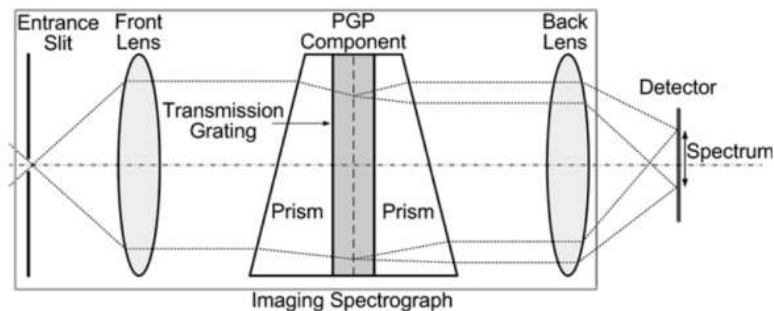


Figure 2.7: Setup of a PGP imaging spectrograph. The incident beam enters through the thin slit, diffracted into separate wavelengths by the PGP component, and focused back onto the detector. Figure taken from [30].

The third hyperspectral image acquisition method, shown in Figure 2.6c, is known as the *area-scanning* or *band sequential* method. One spectral band is acquired over the entire 2D image, and the area is scanned over multiple bandwidths by altering the wavelength dispersion device inside the camera. The final method, shown in 2.6d, is the *single shot*, *non-scanning* or *snapshot* method. As the name suggests, the entire datacube is captured in one instance. However, this can lead to reduced resolution in either the spatial or spectral domain, as it is capturing a 3D datacube with a 2D sensor array [31].

## 2.5.1 Ecotone UHI

The use of UHI sensors was first published in 2013 [32], and has since then been applied to different applications such as underwater mapping [33, 34, 35], underwater archaeology [33, 36], and to determine biophysical properties under the ice [8, 37]. UHIs are mainly used *in situ*, and can be deployed from various marine platforms such as ROVs [34, 36, 38], underwater sleds [26], USVs [35], or even SCUBA divers [39]. We will examine some of these applications in more detail in Chapter 3.

For this study we used the UHI-6, a linescan camera from Ecotone (Trondheim, Norway). The technical specifications are outlined in Table 2.1.

<b>Environmental Specifications</b>	
<b>Depth rating</b>	2000 <i>m</i>
<b>Operating temperature</b>	-5 °C to +35 °C (in water) -5 °C to +25 °C (in air)
<b>Hyperspectral imager</b>	
<b>Spectrograph slit size</b>	80 $\mu\text{m}$
<b>Imager frame rate</b>	Max 100 Hz full resolution, Max 200 Hz if region of interest is reduced
<b>FOV transverse/longitudinal</b>	$\sim 50^\circ / \sim 0.4^\circ$ (In water) $\sim 68^\circ / \sim 0.54^\circ$ (In air)
<b>Camera spatial resolution</b>	1936 spatial pixels
<b>Spectral range</b>	380 – 750 <i>nm</i>
<b>Spectral resolution</b>	5.5 <i>nm</i>
<b>Spectral band count</b>	$\sim 800$
<b>Analog to digital converter (ADC)</b>	12-bit
<b>Exposure time range</b>	1 – 5000 <i>ms</i>
<b>Calibrated for</b>	Radiometric, geometric, and spectral parameters

Table 2.1: Technical specifications of the Scientific UHI-6 OV hyperspectral imager. Compiled from [40].

# Chapter 3

## Previous Works

Light transmittance and the light field under the ice have been areas of study for several decades. The under-ice light environment can be examined by measuring spectral radiance and irradiance to quantify light transmittance through the ice. Radiative transfer models are applied to calculate spectral extinction coefficients and better understand the optics of sea ice. The use of UHI in this area, however, is a recent advancement, and as such very few works in this context exist.

In this section, we provide a brief review of studies that apply UHI to under-ice light analysis, along with other key research focusing on the light field beneath the ice. In Chapter 6 we compare our results to those outlined here.

### 3.1 Under-ice Hyperspectral Imaging for Light Studies

Table 3.1 outlines three main studies existing on under-ice hyperspectral imaging. To our knowledge, these are the only existing studies using a pushbroom hyperspectral camera to research light transmittance through sea ice.

The Multidisciplinary drifting Observatory for the Study of Arctic Climate (MOSAIC) project was a large interdisciplinary research project aiming to characterize the physical properties of the snow and ice cover comprehensively in the central Arctic over an entire annual cycle [1]. Five separate teams focused on the atmosphere, sea ice, ocean, ecosystem, and biogeochemical processes. For this thesis project, specifically the sea ice research is of interest. One of the main goals of the snow and sea ice team was to quantify the partitioning of solar radiation between the snow, the sea ice, and the ocean. Researchers took optical measurements of albedo, transmittance, and light extinction in snow, sea ice, and the underlying water, using a variety of sensors to measure broadband, spectral, or photosynthetically active radiation (PAR). Under-ice radiation measurements were taken by mounting a UHI sensor on an ROV. Measurements with the ROV focused mainly on obtaining a better understanding of the seasonal ice cycle with respect to several aspects: (1) ice draft and bottom topography, (2) the light field beneath the ice, (3) the biophysical properties of the ice and uppermost ocean, and (4) the organisms living in and under the sea ice. Results of the light transmittance measurements are shown in Figure 3.1. The top panel shows the integrated transmittance from 350-920 *nm* along the dive track for five separate dives in July 2020. The bottom panel shows the histogram of light transmittance derived from the corresponding dive in the top panel. Comparing the transmittance between the dives throughout the month shows

Summary	Light Measurements	Mean Ice and Snow Thickness	Platforms	Main Field of Study	Reference
Multidisciplinary project to characterize the physical properties of the snow and ice cover comprehensively in the central Arctic over an entire annual cycle. Spectral transmittance was measured through sea ice using a UHI mounted on an ROV.	Transmittance	<b>Ice:</b> 2.7 m <b>Snow:</b> 0–0.3 m	UHI on ROV; L-arm PAR sensors; fixed sensors at radiation station throughout the seasons	Biology, chemistry, physics	Nicolaus et al [1]
Developing methods using an ROV equipped with a UHI camera to map Arctic kelp forests and sea ice habitats. The mini-ROV-UHI system was used to study macroalgal growth during the Polar Night and under-ice microalgae in extreme environments. Spectral data collected revealed macroalgal growth and photosynthesis during the dark period, as well as a patchy distribution of ice algae biofilms adapted to low-light conditions.	Spectral radiance, total radiance	<b>Ice:</b> 0.36-0.57 m <b>Snow:</b> unknown	UHI on ROV	Biology	Summers [8]
Deployment of a novel under-ice sled system, featuring a pushbroom UHI sensor to capture high-resolution data on sea-ice algae biomass at the ice-water interface. The UHI sensor quantified biological properties through light transmission, offering a non-invasive approach to studying sea-ice environments.	Spectral radiance, spectral irradiance	<b>Ice:</b> 1.8 m±0.01 <b>Snow:</b> none	UHI and hyperspectral radiometer on under-ice sled	Biology	Cimoli et al [26]
<i>Note: Ice and snow thicknesses are given as means or as ranges where possible.</i>					

Table 3.1: Summary of under-ice UHI light measurement studies.

the increasing amount of radiation passing through the sea ice as melting progresses. Additionally, the transmittance distribution shifts from a unimodal distribution with a mode of 0.03 to a bimodal distribution with modes at 0.15 and 0.26. This shift in the distribution indicates a transition from widespread wet, melting snow to a pattern characterized by white ice and melt ponds [1].

The work done for the PhD thesis by Natalie Summers [8] is one of few studies using UHI data to measure transmitted radiance through sea ice. The author focuses mainly on the effects of light on macroalgae under the ice, which includes mapping the transmitted radiance through clean ice (without algae growth), and through ice covered in an algal biofilm. Spectral radiance measurements peaked around  $200 \text{ mW m}^{-2} \text{ sr}^{-1} \text{ nm}^{-1}$  for clean ice (*i.e.* ice without algal biomass), as seen in Figure 3.2. Measurements were taken in early to mid May 2021, and ice thickness was between 0.36-0.57 m.

The project by Cimoli et al [26] focuses on providing a proof of concept of using UHI measurements

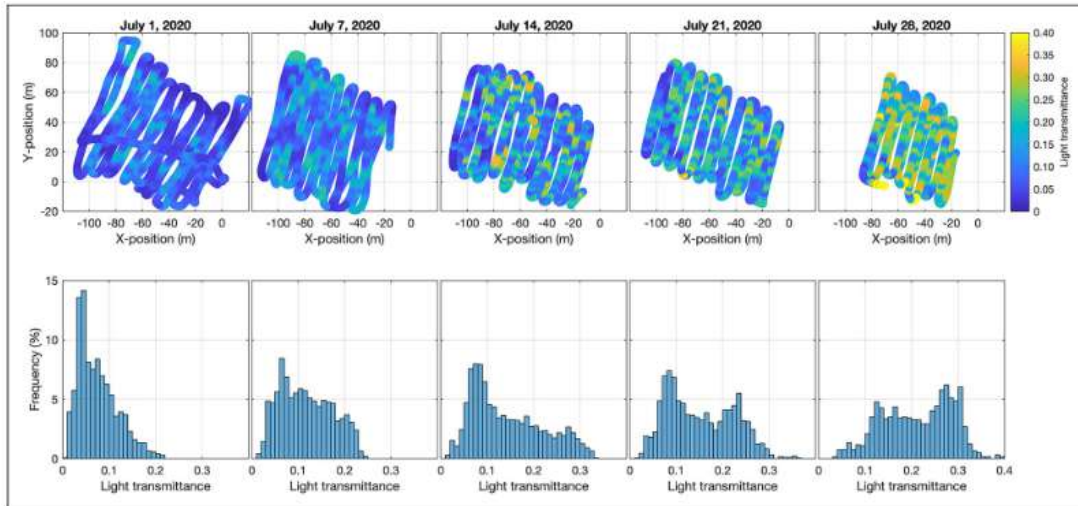


Figure 3.1: Light transmittance measurements from the MOSAiC project. The top panel shows the transmittance along the dive track, and the bottom panel shows the light transmittance distribution for the above dives. Figure taken from [1].

### Spectra from UHI pixels

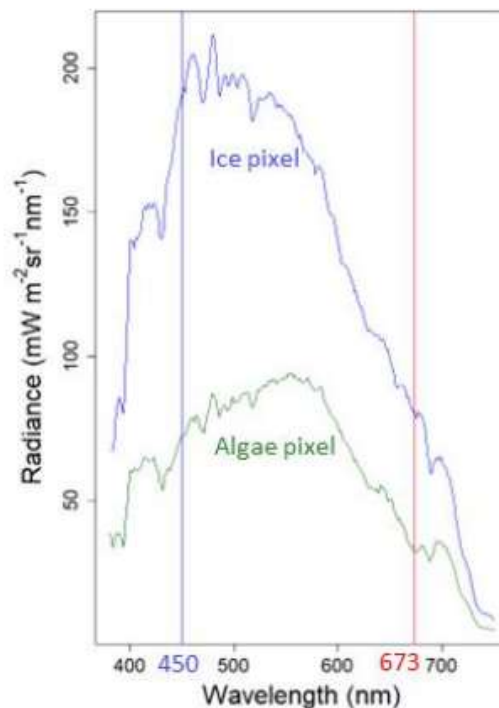


Figure 3.2: Under-ice downwelling radiance measurements from [8].

and photogrammetry to estimate ice algal biomass in a non-invasive manner *in situ*. The authors towed an under-ice sled system mounted with an AISA Kestrel 10 pushbroom hyperspectral imaging camera (AK10) (Specim Spectral Imaging Ltd., Oulu, Finland) and Ramses ACC-VIS hyper-spectral cosine corrected radiometer (TriOS Mess- und Datentechnik GmbH, Rastede, Germany) underneath level ice along a 20 m transect. Measurements were taken in November and December near Cape Evans, Antarctica, under a thick sheet of bare ice measuring approximately 1.8 m.

While the spectral shape of the transmitted radiance closely matches that in [8], the algal biomass below the ice in this study was extremely high, blocking most of the incoming light, and so the magnitudes differ by a factor of almost 100. The transmitted spectral radiance measurements from the hyperspectral camera show that a maximum of approximately  $12 \text{ mW m}^{-2} \text{ sr}^{-1} \text{ nm}^{-1}$  around  $550 \text{ nm}$  reached under the ice. Since our project is not concerned with algal growth under the ice, and our data were collected under ice where no algae layer was present, we will disregard these results for any further comparisons.

### 3.2 Other Under-Ice Light Field Studies

Many other studies concerning light transmittance through sea ice exist (e.g. [17, 22, 23, 24, 41, 42, 43, 44]). We examine a selection of these papers in the following two sections.

Wongpan et al [44] and Lebrun et al [41] examined under-ice light properties using hyperspectral radiometers instead of pushbroom sensors.

Wongpan et al [44] measured light transmittance under the ice in the non-polar Saroma-ko Lagoon in Japan using hyperspectral radiometer sensors to non-invasively estimate the distribution and biomass of sea-ice algae. The study underscores the need for tailored methods for different environments, as Arctic and Antarctic models do not fully apply to the nonpolar Saroma-ko Lagoon.

Lebrun et al [41] analyse Earth System Model (ESM) parameterizations using a dataset of 349 observational records of under-ice light collected across the Northern Hemisphere from studies in Baffin Bay (2015-2016), the Chukchi Sea (2014, 2016), Svalbard (2016, 2018), and Saroma (2019). The Saroma measurements are those taken by the researchers of [44]. The Chukchi Sea measurements correspond to drift ice, and thus are not directly relevant to our study. All data were measured with hyperspectral irradiance radiometers. The main findings showed that snow depth and the presence of melt ponds were significant factors in light transmission, and existing ESMs struggled to accurately predict under-ice light. Results of relevant light transmittance measurements and corresponding ice and snow thicknesses are shown in the first five rows of Table 3.2 below.

No.	Location	Ice Type	Year(s)	$h_i$ [m]	$h_s$ [m]	$T \times 10^{-2}$	Ref
1	Baffin Bay	Fast	2015	$1.21 \pm 0.07$	$0.20 \pm 0.11$	$0.6 \pm 1.8$	[41]
2			2016	$1.28 \pm 0.11$	$0.19 \pm 0.14$	$2.3 \pm 3.2$	[41]
3	Svalbard	Fast (Stf)	2016	$0.63 \pm 0.08$	$0.22 \pm 0.14$	$0.3 \pm 1.4$	[41]
4		Fast (VMf)	2018	$0.51 \pm 0.12$	$0.11 \pm 0.08$	$0.6 \pm 9.0$	[41]
5	Saroma	Fast	2019	$0.49 \pm 0.03$	$0.07 \pm 0.01$	$0.6 \pm 0.1$	[41, 44]
6	Barrow, Alaska	Fast	March 2010	$1.28 \pm 0.06$	$0.22 \pm 0.08$	$0.22 \pm 0.22$	[23]
7		Fast	May 2010	$1.47 \pm 0.06$	$0.27 \pm 0.06$	$0.19 \pm 0.06$	[23]
8		Fast	June 2010	$1.5 \pm 0.02$	$0.07 \pm 0.03$	$4.1 \pm 1.9$	[23]
9	Chukchi Sea Beaufort Sea	Fast	2010, 2011	1.3	0.0	3 to 22	[12]

Note on ice types: Stf=Storfjorden, VMf=Van Mijenfjorden. Fast=landfast level ice.  
Mean  $\pm$  standard deviation (SD) is given for  $h_i$ ,  $h_s$  and  $T$  where it is known. For entry 9 SD is unknown.

Table 3.2: Summary of snow, ice, and light transmittance observations from non-UHI studies.

Figure 3.3, taken from [22], summarizes the spectral light transmittance for several different ice types and surface conditions from measurements made by Light et al [42] and Nicolaus et al [23]. Transmittance is heavily influenced by snow and ice thickness [22], and as a result, under-ice variations in light intensity span several orders of magnitude [41, 17], as can be seen in Figure 3.3.

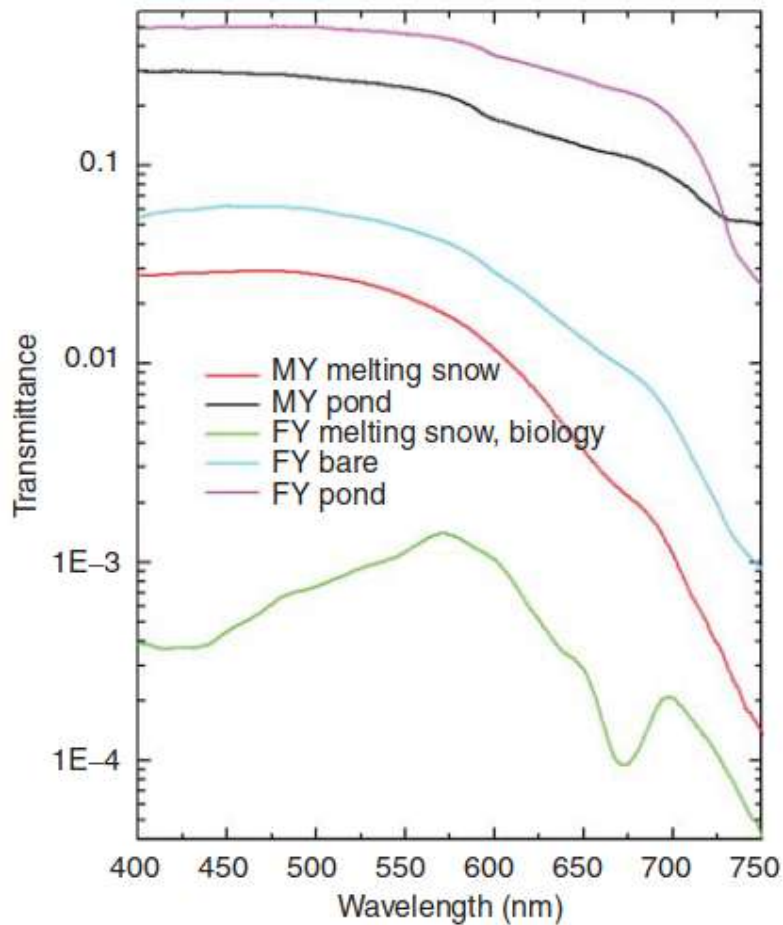


Figure 3.3: Spectral transmittance plots for selected cases. Details of the cases are as follows: multi-year (MY) melting snow had 10 *cm* of snow over 186 *cm* of ice; MY pond had 25 *cm* of water over 133 *cm* of ice; first-year (FY) snow has 11 *cm* of snow over 106 *cm* of ice with a flourishing ice algae layer; FY bare had 149 *cm* of ice; and FY pond had 8 *cm* of water over 112 *cm* of ice. Image and caption taken from [22].

The under-ice measurements in [23] were taken simultaneously with incident solar irradiance measurements, using upward-looking Ramses spectral radiometers with advanced cosine collectors (Ramses ACC, Trios GmbH, Rastede, Germany). Integrated transmitted light measurements, as well as corresponding ice and snow thicknesses, are summarized in rows 6-8 of Table 3.2.

### 3.3 Sea Ice Radiative Transfer Models

Radiative transfer models are essential in calculating spectral extinction coefficients and understanding light transmittance through sea ice. Several radiative transfer models exist, the simplest being the exponential decay model given by (2.7) in Chapter 2.

Figure 3.4.a and 3.4.b outline spectral extinction coefficients that have been compiled by Perovich in [11, 22]. Figure 3.4.a shows spectral extinction coefficients for dry and wet snow, and for bare and ponded first-year and multi-year sea ice from data collected in [45, 13, 42]. Figure 3.4.b shows the coefficients for nine specific cases: dry snow, melting snow, ice below the eutectic point (*i.e.* temperatures low enough

for both the ice and dissolved salts to solidify), the surface scattering layer of white ice, the interior of white ice, cold blue ice, melting blue ice, bubble-free fresh ice, and clear Arctic water. These extinction coefficients were calculated using a two-stream radiative transfer model from Grenfell and Maykut [45] and Perovich and Grenfell [13]:

$$E_d(z, \lambda) = \frac{E_0 \sinh[\kappa_\lambda(h-z) + \sinh^{-1}(\kappa_\lambda/r_\lambda)]}{\sinh(C)} \quad (3.1)$$

$$E_u(z, \lambda) = \frac{E_0 \sinh[\kappa_\lambda(h-z)]}{\sinh(C)} \quad (3.2)$$

where  $r_\lambda$  is the volume reflectance coefficient,  $h$  the ice thickness,  $z$  the depth in the ice, and  $C = \kappa_\lambda h + \sinh^{-1}(\kappa_\lambda/r_\lambda)$ . Equations 3.1 and 3.2 can be inverted to obtain  $\kappa_\lambda$  and  $r_\lambda$ .

For optically thick ice (*i.e.* as ice thickness approaches  $\infty$ ) the downwelling irradiance model reduces to (2.7) with  $\alpha_\lambda=0$ . Similarly, the upwelling irradiance model reduces to 2.7 but with a multiplication of  $\alpha_\lambda$  instead of  $(1-\alpha_\lambda)$ .

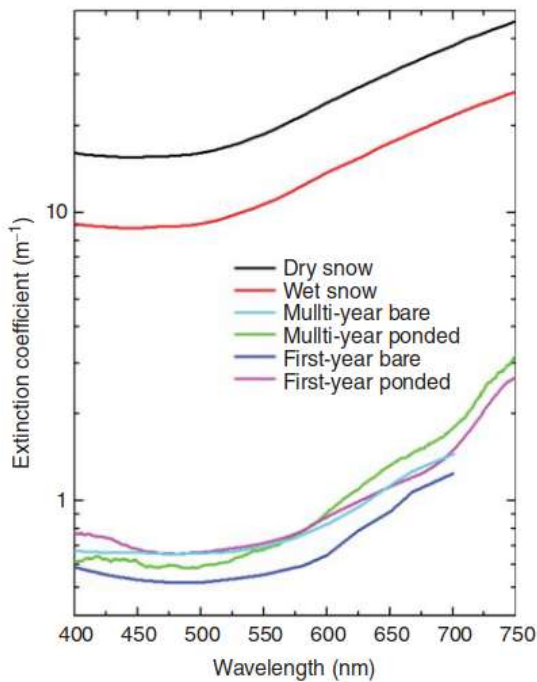


Figure 3.4.a: Spectral extinction coefficients for wet and dry snow, and ponded and bare first-year ice and multi-year ice. Figure taken from [22].

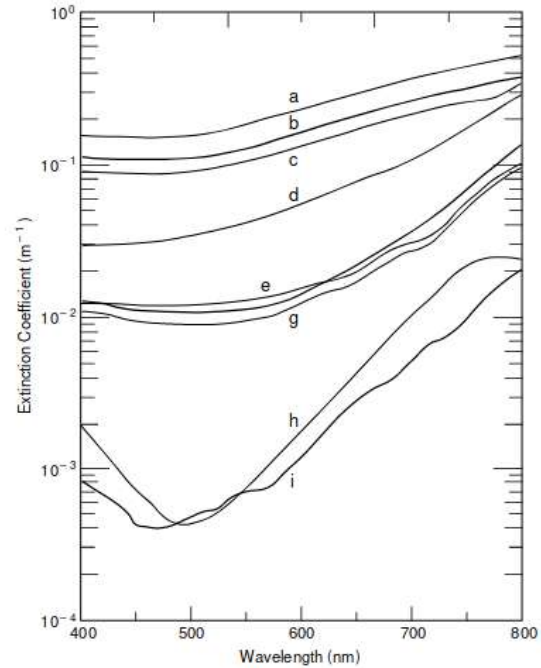


Figure 3.4.b: Spectral extinction coefficients for nine distinct cases: a) dry snow, b) ice below the eutectic point with solid salts present, c) melting snow, d) surface scattering layer of white ice, e) the interior of white ice, f) cold blue ice, g) melting blue ice, h) bubble-free fresh ice, and i) clear Arctic water. Figure taken from [11].

Figure 3.4: Spectral extinction coefficients calculated for various snow and ice conditions, compiled in two papers by Perovich [11, 22]. The most relevant data for our study are the dry snow, first-year bare ice, and cold blue ice.

The extinction coefficients vary by up to two orders of magnitude, highlighting the significant differences in attenuation across various snow and ice types. In the 400-500 nm range, sea ice and snow exhibit relatively stable values, followed by a marked increase in attenuation at longer wavelengths. The greatest

attenuation occurs in cold, dry snow.

Nicolaus and Katlein [24] applied (2.7) without the spectral albedo  $\alpha_\lambda$  term:

$$E(z, \lambda) = E_0(\lambda)e^{-\kappa_\lambda z} \quad (3.3)$$

They then used the calculated extinction coefficients to correct the fluxes at the ice-water interface as follows:

$$T_{E\text{corrected}}(\lambda) = \frac{T_{E\text{measured}}(\lambda)}{e^{-\kappa_\lambda \cdot d}} \quad (3.4)$$

where  $d$  is the distance to the ice.

Katlein et al [17] apply (2.7) to show that light transmittance can be inferred from ice thickness and albedo distribution. The authors combined ice thickness and albedo under-ice visual measurements and 3D topography measurements from a multibeam sonar, with aerial camera images of the ice surface conditions. They extracted the surface thickness from the under-ice measurements, and calculated the albedo from the aerial images. The authors derived a bulk extinction coefficient of  $1.5 \text{ m}^{-1}$ .

Light et al [12] calculated spectral extinction coefficients within the ice using spectral downwelling irradiances. They lowered a vertically resolved downwelling irradiance sensor through small boreholes and measured irradiance every  $0.1 \text{ m}$ . Relative downwelling irradiance at  $500 \text{ nm}$  as a function of depth are shown in Figure 3.5a. The authors then applied (3.5), obtaining the extinction coefficients shown in Figure 3.5b.

$$\kappa_\lambda(z) = \frac{-2}{E(\lambda, z_2) + E(\lambda, z_1)} \frac{E(\lambda, z_2) - E(\lambda, z_1)}{(z_2 - z_1)} \quad (3.5)$$

The depth  $z = (z_1 + z_2)/2$ , and  $E(\lambda, z_i)$  is the downwelling irradiance at wavelength  $\lambda$  and depth  $z_i$ .

The above mentioned sea ice radiative transfer models all rely on the assumption of isotropic scattering. However, recent studies by Katlein, Nicolaus, and Petrich [15] show that this assumption is not generally valid, and leads to significant errors when converting from radiance to irradiance. Instead of the common conversion given in (2.4), they introduce a value  $C$ , which is the ratio of irradiance  $E(\lambda)$  to radiance  $L(\lambda)$ . When rearranged for  $E(\lambda)$ , this gives the following:

$$E(\lambda) = CL(\lambda) \quad (3.6)$$

The authors found that  $C$  could be described by the linear relationship

$$C = 2.5 - 2\gamma \quad (3.7)$$

where  $\gamma$  is the anisotropic scattering coefficient. This implies that even for isotropic scattering ( $\gamma = 0$ ), the original (2.4) gives irradiance values that are much too high.

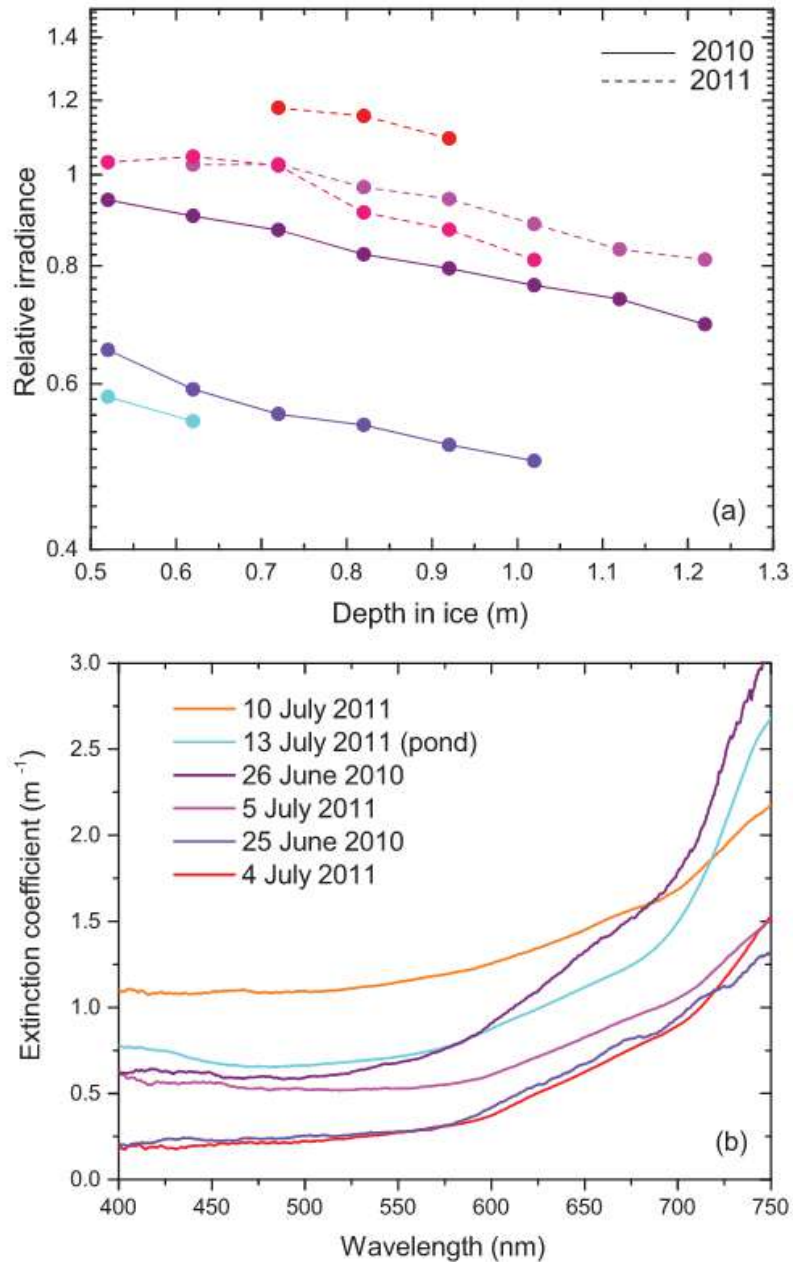


Figure 3.5: (a) Relative downwelling irradiance at 500  $nm$  as a function of depth, and (b) spectral irradiance extinction coefficients inferred from the irradiance profiles. Figure taken from [12].

### 3.4 Literature Gaps

Sea ice plays a huge role in climate regulation, and to better understand the exact effects it is important to understand the atmosphere and polar ocean interactions. As demonstrated in the section above, sea ice optics have been widely studied, but knowledge about the optical properties of sea ice and radiative transfer through sea ice is still limited. This is largely due to the remoteness and harsh climate of the polar regions making it difficult to access the under-ice environment to gather data.

Furthermore, UHI is still a relatively new technology. Up until now, light related hyperspectral data have most commonly been used to study biophysical [8, 26] and biochemical [44] properties under the ice.

Ice thickness has been used to infer light penetration [17], but no research exists using UHI to determine ice thickness.

The aim of this project is to address these gaps, and to further the understanding of the correlation of sea ice thickness and the under-ice light climate, using UHI data.

# Chapter 4

## Methodology

This chapter details the methodology used to complete this study. Since the project consists of data collection as well as data processing and analysis, we separate the chapter into two main sections.

### 4.1 Data Collection

The first major task of this project was to obtain data from above and below the sea ice. This was done on a multi-day field excursion to the Svea field station in Van Mijenfjorden, Svalbard.

The robotic platform was mostly disassembled for the transport from Trondheim to Svalbard, and had to be reassembled and retested upon arrival in Longyearbyen. We ran an initial Arctic field test in the Longyearbyen harbour and made final adjustments (Figure 4.1) before the trip to Svea.

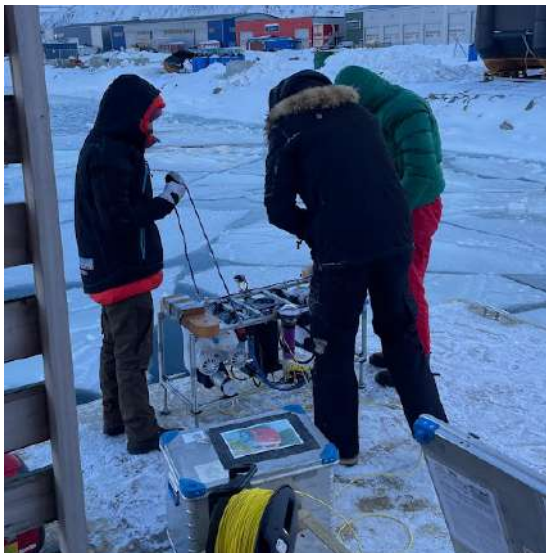


Figure 4.1: Initial field test on Svalbard in Longyearbyen. Air temperature  $-20^{\circ}\text{C}$ .



Figure 4.2: Packaging of the DBE for the snow scooter sledge.

To safely transport the platform to the Svea field-station, we constructed a padded, insulated box, seen in Figure 4.2, to protect the platform and instruments from the cold temperatures and uneven terrain on the five-hour scooter trip.

### 4.1.1 Double Blueye Robotic Platform

The Double Blueye (DBE) robotic platform used for the data collection consists of two Blueye ROVs and three underwater sensors. The concept of the DBE was first introduced by Løvås et al [38], and extended for our research.

The two Blueye robots were mounted onto a lightweight metal frame with the Ecotone UHI (Trondheim, Norway) placed between them. The UHI also contains an integrated subsea altimeter. We added a Doppler Velocity Log (DVL) from Waterlinked (Trondheim, Norway) for underwater navigation purposes, and a KELDAN light source (Bruegg, Switzerland) modified with a LED Module Hyperspectral 80W for additional illumination under the ice. The entire system can be seen in Figure 4.3.

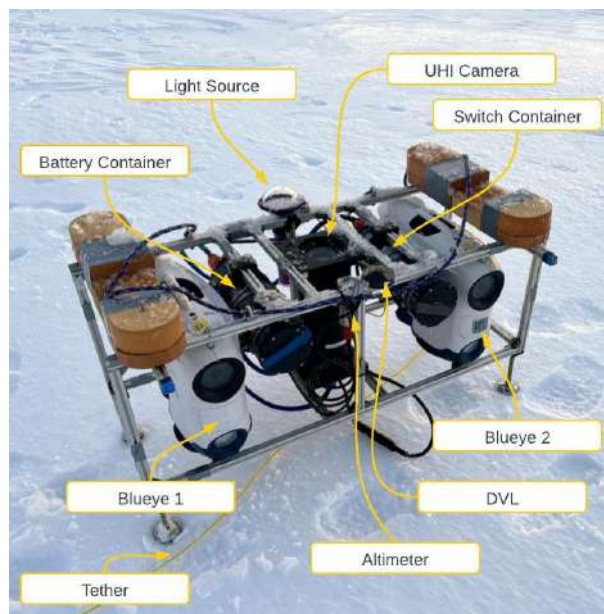


Figure 4.3: Schematic representation of the DBE system setup, showing key components including the light source, DVL, altimeter, battery container, switch container, tether, UHI camera, and Blueye 1 and Blueye 2 underwater vehicles.

The Blueye ROVs, and KELDAN lamp each come with their own power supplies, so only the DVL, altimeter, and UHI camera require an external power source. Both were connected to a Bluerobotics (Torrance, California) battery, housed in a watertight container.

We managed the networking between the two Blueyes by merging the communication lines of the two ROVs. The ROVs use a network multi-access method known as a Carrier Sense Multiple Access with Collision Avoidance (CSMA-CA). The nodes listen for traffic along the transmission line, and begin transmitting only when the channel is sensed as empty. When the line is idle, the nodes transmit their entire data packets at once. This collision-avoidance networking method allowed us to combine the communication lines of the two ROVs.

The UHI camera data are sent via a networking switch installed in a watertight container. This switch connects to the Blueye tether via an ethernet-to-serial connector, which runs up to the surface and connects to the Blueye reel, configured as a Wi-Fi access point. This allows laptops and phones on the surface to connect to the setup. The DVL shares the communication pipeline with the UHI, and is connected to the network via the same switch.

The entire DBE networking setup is outlined in Figure 4.4.

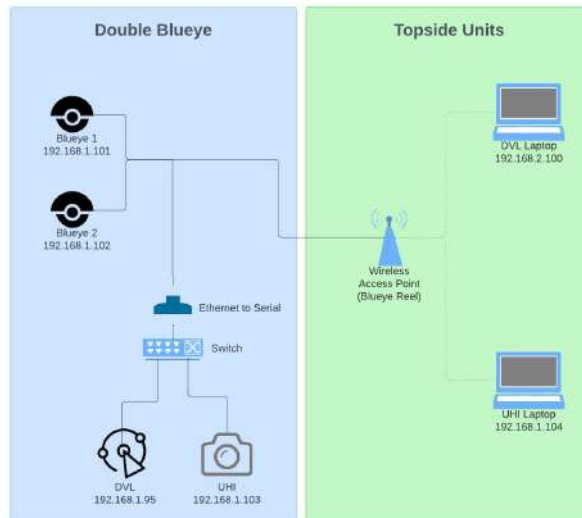


Figure 4.4: Networking setup of the DBE platform.

The UHI laptop was set up with the UHI processing software *Immersion*, provided by Ecotone (Trondheim, Norway). The software can be seen on the right laptop in Figure 4.5.b. The software shows the live hyperspectral data, visualized as RGB imagery, the UHI's RGB camera feed, and the optical signature of the hyperspectral data.

The DVL laptop runs the script for the DVL, and the program used to pilot the DBE, seen on the left laptop in Figure 4.5.b. The program is connected to an X-Box controller, which can be used to fly the ROV, as seen in Figure 4.5.a.



Figure 4.5.a: ROV piloting station. The DBE is being controlled through an X-Box controller (front), while the SBE is being controlled through the Blueeye phone app (middle).



Figure 4.5.b: Topside units of DBE setup. The laptop on the left shows the DVL script and RGB camera feed of the robot. This laptop is also used to control the DBE. The *Immersion* software is running on the right laptop, showing the live hyperspectral data, visualized as RGB imagery, the UHI's RGB camera feed, and the optical signature of the hyperspectral data.

Figure 4.5: ROV piloting station.

## 4.1.2 Test Site Preparation

The field excursion to Van Mijenfjorden took place March 19 - 22, 2024 in collaboration with the University Centre in Svalbard (UNIS) Sea Ice Mechanics and Physics course (AT-311). Upon arriving at Svea, the DBE was unloaded, reassembled, and tested, to ensure that no damage occurred during transport.

The first morning was spent preparing the test site for the underwater data collection. We cut a hole of approximately  $1\text{ m} \times 1.5\text{ m}$  through which the DBE could be lowered into the water, and cleared an ice patch of similar dimensions approximately  $30\text{ m}$  from the launch hole. An ice saw was driven through the ice to serve as an underwater marker for the ROV. Figure 4.7.b shows the DBE hovering under the cleared ice, with the ice saw visible towards the left of the hole. The stretch from the launch hole to this cleared patch of ice served as the transect under which to fly the DBE to obtain the under-ice data. The area around the transect was fenced off, to ensure the snow stayed undisturbed. To shield the equipment and ourselves from the  $-25^{\circ}\text{C}$  air temperatures, and to maintain a constant-temperature environment for the equipment, we set up an Ice Hotel fishing tent above the launch hole (Figures 4.6.a and 4.7.a). A schematic of the area can be see in Figure 4.6.b.



Figure 4.6.a: Ice hotel set up over launch hole with testing area fenced off.

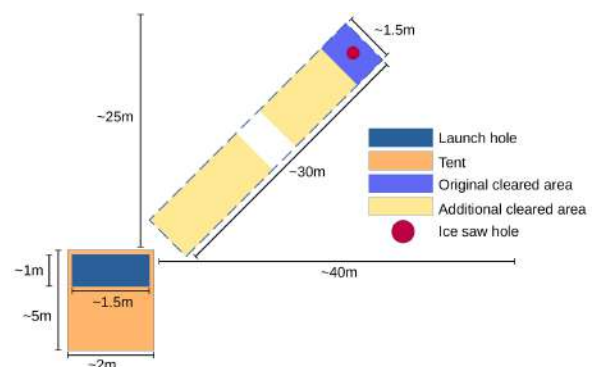


Figure 4.6.b: Schematic representation of Svea test site.

Figure 4.6: Svea test site.



Figure 4.7.a: Launching the DBE through the hole in the tent.



Figure 4.7.b: DBE hovering under hole at end of transect. Ice saw can be seen at the edge of the hole.

Figure 4.7: DBE launch (4.7.a) and under-ice operation (4.7.b).

### 4.1.3 Double Blueeye Measurements

The goal of the under-ice data collection was to complete several flights with the DBE from the launch hole to the end of the transect, while maintaining a constant speed and altitude. Due to networking issues, these experiments were limited to one day.

To obtain above-ice radiance measurements we pointed the UHI upwards to capture the incoming radiance from the clear sky, and downwards at a Spectralon (Labsphere Inc, North Sutton, USA) reference plate placed on undisturbed snow to capture the reflected radiance. The Spectralon can reflect up to 99% of all incident light across the UV, visible, and near infrared spectrum, making it an ideal reference standard [29]. Figure 4.8 shows the reflected radiance being measured with the UHI.

We took a total of four above-ice measurements spaced throughout the day, as summarized in Table 4.1. The consistently clear conditions, with no cloud cover, allowed us to interpolate the above-ice radiance for the entire day.



Figure 4.8: Reflected radiance measurements; the UHI is pointed down, towards the Spectralon reference plate.



Figure 4.9: Cleared runway for DBE to follow, as seen from starting point of transect.

Measurement No.	Measurement Type	Time	Comments
1	Sky	10:46	Before first run
	Snow	10:48	
2	Sky	12:55	Before lunch
	Snow	12:57	
3	Sky	16:42	After lunch
	Snow	16:43	
4	Sky	18:24	After last run
	Snow	18:25	

Table 4.1: Above-ice measurement timestamps.

Between above-ice measurements 1 and 2, and 3 and 4, we deployed the DBE to collect measurements under the ice. A total of six flights (also referred to as runs, trials, or transects) were completed. During the first three trials, navigational challenges and equipment malfunctions prevented the completion of the transect: the X-Box controller used to manoeuvre the DBE repeatedly powered off due to the cold; poor under ice visibility made localization difficult; and navigational drift in the DVL output (as seen in Figure 4.10) further complicated smooth piloting. To assist with navigation, we deployed a Single Blueye (SBE) to act as a guide vessel for the DBE. As of the fourth trial, we managed to successfully fly the DBE to the end of the transect, locate the ice saw, and return to the launch point. The three successful flights are listed in Table 4.2.

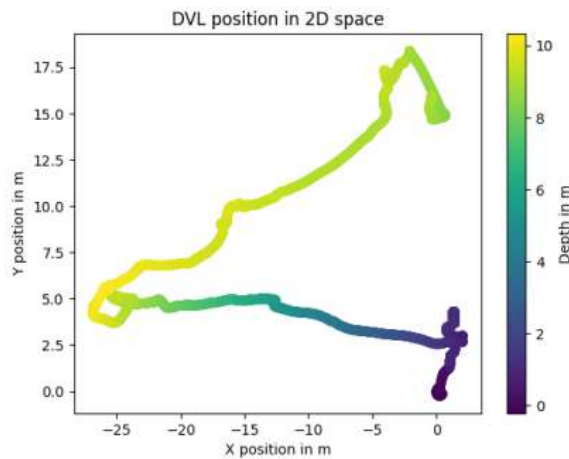


Figure 4.10: Plot of DVL track from run 6. The first measurement taken by the DVL, underneath the launch hole, is set as  $x = 0$ ,  $y = 0$ ,  $Depth = 0$ . The last measurement should match the starting position in both  $x$  and  $y$  coordinates, since the starting and stopping locations were both directly beneath the launch hole.

Flight No.	Start Time	End Time	Snow-covered	Comments
4	12:37	12:49	Yes	-
5	16:57	17:18	Yes	Light on during run
6	17:57	18:20	Partially	Low incoming light

Table 4.2: Overview of successful DBE flights.

For the final run, we cleared a 0.4 m wide trench from the launch hole to the end of the transect, as shown in Figure 4.9. This aided with the localization and manoeuvring under the ice, creating a "runway" for the ROV to follow. It also simplified the comparison of light attenuation under snow-covered and bare ice. One section of 2.5 m was left covered in snow, 12.5 m from the start of the transect.

Snow depth measurements along the transect are shown in Table 4.3. All snow depth measurements were taken to the right of the runway, unless otherwise stated. An ice thickness of 0.62 m was measured at the launch hole.

While it was not possible to take direct ice measurements along the transect, Table 4.4 shows snow and ice measurements from the immediate surrounding area. Given the level ice and uniform snow conditions, it is reasonable to assume that the ice thickness along the transect closely aligns with the values presented in Table 4.4.

No.	Distance [m]	Snow Depth [m]	Additional Comments
1.	0.0	0.20	Ice thickness: 0.62 <i>m</i>
2.	2.0	0.16	–
3.	5.0	0.15	–
4.	8.0	0.10	–
5.	12.0	0.14	–
6.	12.5	0.08 – 0.13	snow on runway – variable depths, disturbed snow
7.	15.0	0.23	start of second part of transect
8.	15.0	0.27	max depth from blown snow
9.	18.0	0.20	–
10.	22.0	0.25	–
11.	26.0	0.22	right of runway
12.	26.0	0.21	left of runway
13.	28.0	0.20	–
14.	29.0	0.20	–
15.	30.0	0.18	max depth, variable depths, disturbed snow
16.	30.0	0.13	min depth
17.	31.0	0.21	measurement next to larger area cleared for hole

Table 4.3: Snow Depth measurements along the ROV transect. Distance refers to the distance along the transect from the launch hole. All snow depth measurements were taken to the right of the runway, unless otherwise stated.

No.	Ice Thickness [m]	Snow Thickness [m]	Freeboard [m]	Temperature [°C]
1.	0.63	0.21	0.01	-8.9
2.	0.65	0.21	-0.015	-6.2
3.	0.60	0.19	0.0	-10.2
4.	0.66	0.24	-0.005	-9.4
5.	0.65	0.25	-0.02	-6.7
6.	0.67	0.25	-0.01	-7.7
7.	0.71	0.22	0.0	-7.7
8.	0.70	0.22	0.005	-8.9
9.	0.68	0.24	-0.01	-9.2
10.	0.65	0.23	0.0	-8.9
11.	0.65	0.21	-0.005	-8.4
12.	0.66	0.21	0.0	-9.1
13.	0.63	0.26	-0.015	-8.0
14.	0.57	0.22	0.0	-9.3
15.	0.64	0.20	0.01	-8.7

Table 4.4: Ice and snow thickness measurements in surrounding area. Measurements were taken 100 *m* apart; measurements 1-7 were taken in a line going south from the tents, and 8-15 going back north towards the tents approximately 50 *m* left of first measurements.

## 4.2 Data Processing

Following data collection, the UHI files were processed to obtain spectral radiance and irradiance measurements, as well as spectral extinction coefficients for ice and snow.

### 4.2.1 UHI Data Calibration

The raw recorded UHI data are initially stored as .h5 files on the internal hard drive of the sensor. To process the data, the .h5 files have to be exported to a laptop over the ethernet connection. Each flight is stored in files of approximately 500MB, with the following file name format: **uhi\_yyyyymmdd\_hhmmss\_n**,

where the time **hhmmss** is in UTC time, and **n** refers to the file number. The local time is UTC+1h.

To analyse the data, we first needed to convert the raw UHI data to a usable format, specifically, spectral radiance. The conversion from Digital Number (DN) to spectral radiance  $L(\lambda)$  is generally as follows:

$$L(\lambda) = (DN - Offset) * Gain \quad (4.1)$$

where *Offset* accounts for noise in the sensor, and the *Gain* is estimated by radiometric calibration. The calibration determines how sensitive the sensor is when converting from digital counts to physical radiance [40].

The following is the conversion formula provided by Ecotone AS (Trondheim, Norway):

$$L(\lambda) = \frac{DN - darkframe}{radiometric * t_{exp}} \quad (4.2)$$

During the factory calibration of the Ecotone UHI (Trondheim, Norway), the radiometric frame is defined as  $(DN - Offset)/L/t_{exp}$ , measured in  $\mu W cm^{-2} sr^{-1} nm^{-1}$ .

Comparing with (4.1), we see that the *Offset* is the *darkframe*, and the *Gain* is  $1/radiometric$ . The division by exposure time  $t_{exp}$  is necessary to compute the spectral radiance independent of the camera's exposure settings, and thus representing the actual radiance. The exposure time has been converted from milliseconds to seconds. The *darkframe* and *radiometric* data are included in the UHI calibration files, provided by Ecotone AS (Trondheim, Norway).

It is also possible to perform the conversion directly in Immersion, and the results of (4.2) were verified using the software.

However, while the conversion from the software and the conversion using (4.2) output the same results, the converted radiance was too high by a factor of 100, when comparing to literature values [46, 23]. During the calibration of the UHI-4 (Ecotone, AS), a small aperture was used by mistake, which introduced a factor of 100 (N. Summers, author of [8], personal communication, August 1, 2024). We assume the same error occurred with the UHI-6, and thus update (4.2) as follows:

$$L(\lambda) = \frac{DN - darkframe}{radiometric * t_{exp}} * \frac{1}{100} \quad (4.3)$$

To convert from  $\mu W cm^{-2} sr^{-1} nm^{-1}$  to  $W m^{-2} sr^{-1} nm^{-1}$  the result is again divided by 100.

To obtain the most accurate results, we compare data from bare ice and snow-covered ice taken under the same light conditions and altitude. The UHI data are rendered as images, allowing us to identify sections without snow. The three subfigures in Figure 4.11 are rendered from a representative data segment taken from the fourth trial. Figures 4.11.a and 4.11.b show a pseudo RGB visualization and a representation of the image using only one waveband. The pseudo RGB image is created by extracting three isolated wavelengths, which are then normalized and stacked. Figure 4.11.a, uses wavelengths 590 nm, 565 nm and 440 nm, as these correspond to the red, green, and blue wavelengths that the human eye is most sensitive to [47]. Figure 4.11.b is the visualization using only a single wavelength. We chose  $\lambda=640 nm$  empirically, as this resulted in high contrast in the image. The last image, Figure 4.11.c, is a greyscale rendering of the same data. Sea ice image analysis is often completed in greyscale, given

the lack of colour in detecting white sea ice on a dark ocean [28].

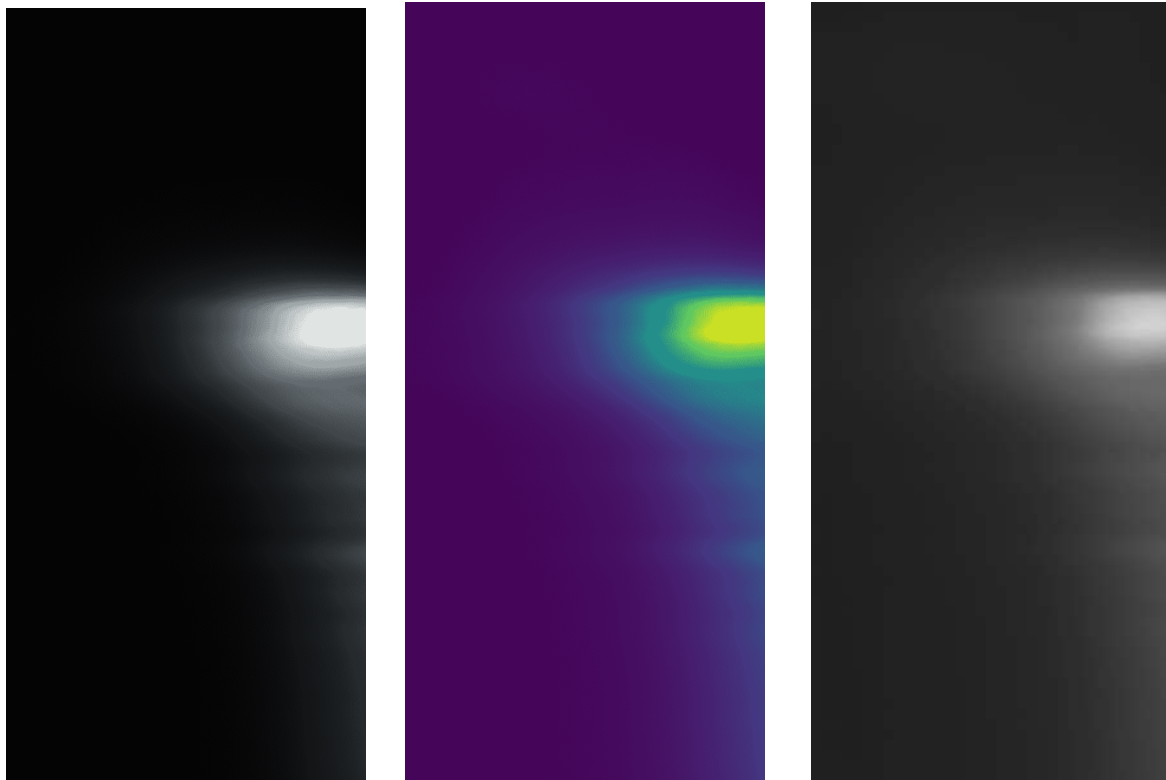


Figure 4.11.a: RGB

Figure 4.11.b:  $\lambda=640 \text{ nm}$

Figure 4.11.c: Greyscale

Figure 4.11: UHI data image renderings

As seen in Figure 4.11, the three image representations highlight different information - the edges of the bare ice patch in the RGB visualization are clear, while in the greyscale image they are softer and more blurred. In the visualization using  $\lambda=640 \text{ nm}$ , it is easier to notice the small differences in light below the bright, cleared patch in the image.

Generating images for all flights, we identified areas of snow-covered ice and bare ice. For the spectral analysis, it was then possible to look at subsections of the same part of the run, guaranteeing the same incoming radiance, same ice thickness, and the same ROV altitude.

## 4.2.2 Radiance and Irradiance Calculations

To verify the accuracy of the measurements, we conducted an initial validation check. Figure 4.12 shows a comparison of incoming, reflected, and transmitted spectral radiance measurements, taken shortly before sunset. The incoming measurements correspond to row 4 in Table 4.1, and transmitted measurements are from flight 6 in Table 4.2. For transmitted measurements, we compared sections of both bare and snow-covered ice, as transmittance is expected to decrease significantly with snow cover [11]. Approximately 10-15% of light passes through bare ice, whereas almost no light penetrates snow-covered ice. These results coincides with previous findings in [11, 17].

The top plot in Figure 4.12 shows the mean spectral radiance of the incoming, reflected, and the two transmitted radiance measurements, as well as the corresponding standard deviations. The mean is taken across the two spatial dimensions of the hyperspectral data. All four curves have comparable

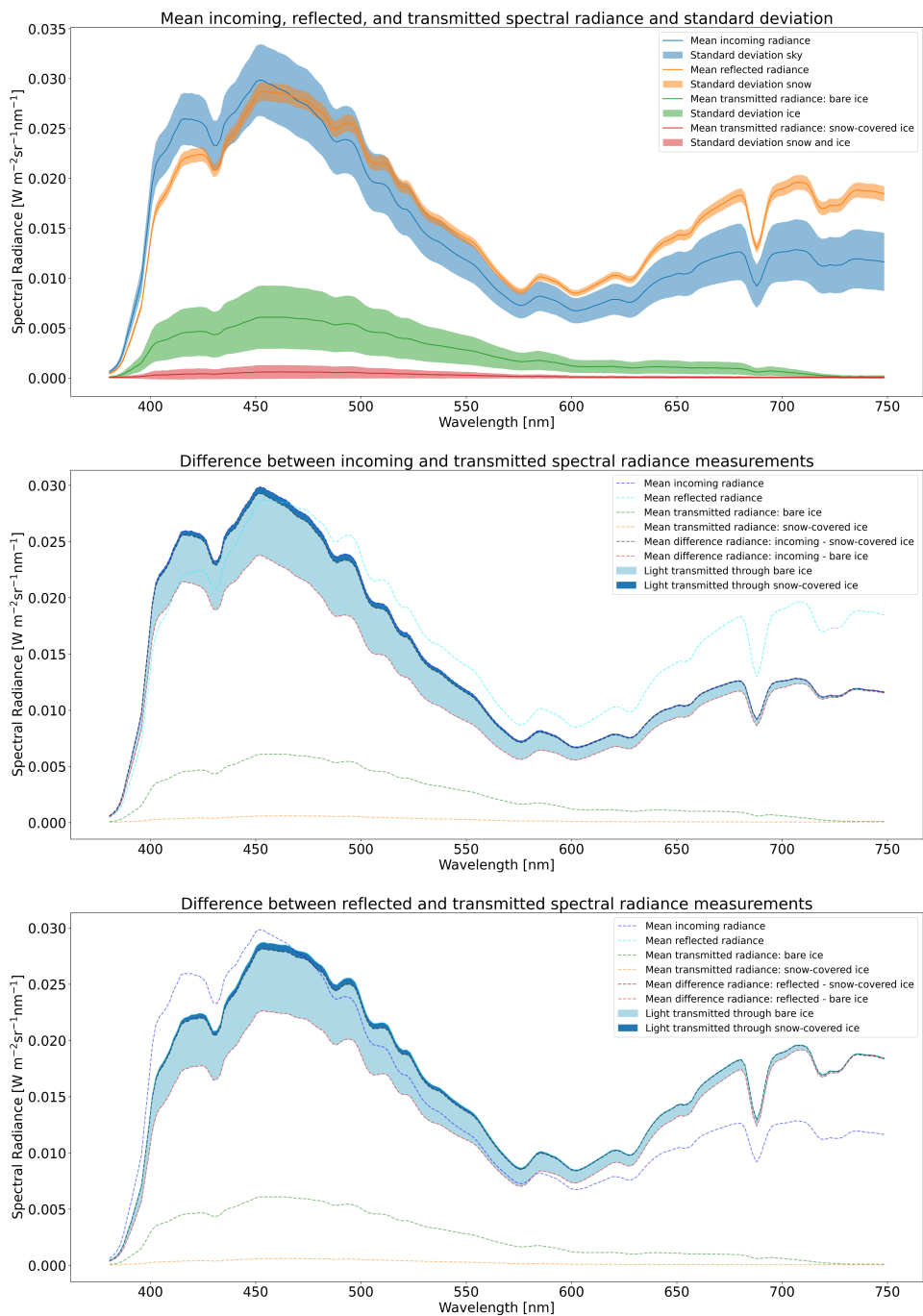


Figure 4.12: Spectral radiance measurements used to validate the data. *Top*: Mean incoming, reflected, and transmitted spectral radiance. Standard deviations are shown by the shaded area above and below each mean spectrum. *Middle*: Difference in radiance between incoming and transmitted measurements. *Bottom*: Difference in radiance between reflected and transmitted measurements. For each of the bottom two plots the light blue shaded area shows the light transmitted through bare ice, and the dark blue shaded area represents the light transmitted through snow-covered ice.

spectral signatures with peaks near 450 nm, corresponding to blue light, but it is easy to see that much of the light is blocked by the bare ice, and even more by snow-covered ice. While the incoming and reflected spectral radiance peak at approximately  $0.3 \text{ W m}^{-2} \text{ sr}^{-1} \text{ nm}^{-1}$ , the spectral radiance transmitted through bare ice (green line) is reduced to  $0.06 \text{ W m}^{-2} \text{ sr}^{-1} \text{ nm}^{-1}$ , and the spectral radiance through snow-covered ice (red line) barely reaches above  $0 \text{ W m}^{-2} \text{ sr}^{-1} \text{ nm}^{-1}$  in the blue waveband range. For the green and red wavelengths, both the bare and snow-covered ice block almost all of the light passing through. The spectral radiance of the incoming light measurement shows a slight increase from the green to red wavelengths, while the reflected radiance increases significantly with the longer wavelengths. This increase in the red spectrum can be explained by the low solar elevation at sunset (around  $1.13^\circ$  at the time of the measurement [48]), which causes sunlight to travel through a longer atmospheric path. The shorter, blue wavelengths scatter more efficiently in the atmosphere, leaving the longer, red wavelengths to dominate the direct radiation reaching the surface [49].

Since the Spectralon reference standard reflects up to 99% of incident light, we expect the incoming and reflected light measurements to be similar. A reflected radiance higher than the incoming radiance, however, is not physically possible, and indicates a likely measurement error. Since both measurements were taken manually with the DBE, the discrepancy is likely due to the tilt angle of the camera relative to the reference standard during the downward measurement. If the camera was not pointed exactly 180 degrees toward the Spectralon block (*i.e.* at a perfect nadir angle), the rays would strike the surface at an oblique angle, spreading the light over a larger area compared to the nadir view. This angular deviation could cause additional light to be reflected from the surrounding snow toward the sensor, falsely elevating the reflected radiance. The reflected spectral and total irradiance from two trials are calculated later in this section for comparison with the incoming measurements, but these measurements are not used in any subsequent calculations or analyses.

In the second plot, the spectral radiance above and below the ice are compared directly. The mean spectra are shown again, and the black dashed line shows the difference between the incoming radiance measured above the ice and the radiance under snow-covered ice. The dark blue fill between the blue dashed line (mean incoming spectral radiance) and the black dashed line therefore represents the amount of light passing through the snow-covered ice.

The light and dark blue fills combined, between the dark blue and red dashed lines, represent the amount of light transmitted through the bare ice. This area is much larger than the area of just the snow-covered ice, as to be expected, as much more light can pass through snow-free sea ice than through snow-covered sea ice. This is partially due to the high albedo of the snow (normally ranging between 0.7-0.9 [11]), since much of the light is immediately reflected.

The last plot in Figure 4.12 is similar to the middle one, but it compares the reflected radiance instead of the transmitted radiance to the incoming radiance. By inspection, the results show a close resemblance.

With the initial data appearing as expected, except for the higher reflected radiance at longer wavelengths, we visualized and compared the spectral radiance and irradiance for snow-covered and bare ice data segments from run 4 and 6.

Figure 4.13 shows the incoming and transmitted radiance measured by the UHI for measurements taken from run 4. Figure 4.13.a shows the incoming radiance in dark blue, and the reflected radiance in light blue. The plot legend shows the file name of the plotted data (*i.e.* UTC time) with a suffix to identify the type of measurement - **incoming** or **reflected** for the above-ice measurements, and **snow** for measurements taken under snow-covered ice. Measurements under bare ice have no suffix.

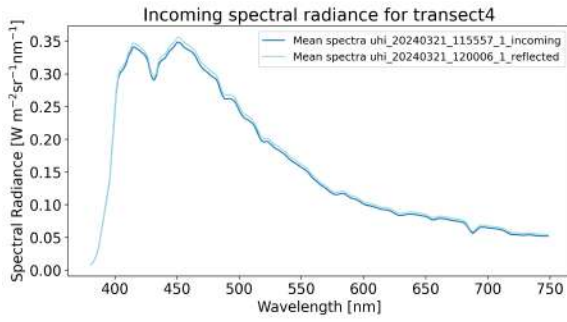


Figure 4.13.a: Incoming (dark blue) and reflected (light blue) spectral radiance for flight 4.

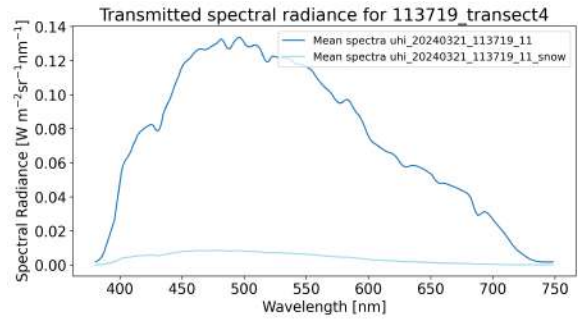


Figure 4.13.b: Transmitted spectral radiance through bare (dark blue) and snow-covered (light blue) ice for flight 4.

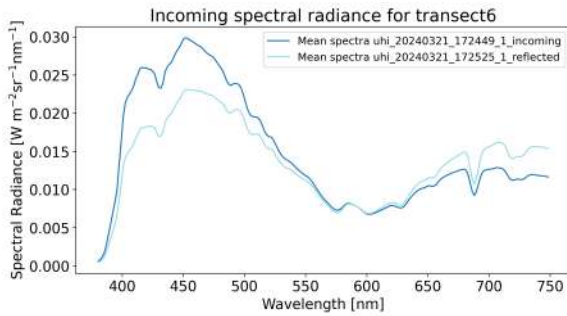


Figure 4.13.c: Incoming (dark blue) and reflected (light blue) spectral radiance for flight 6.

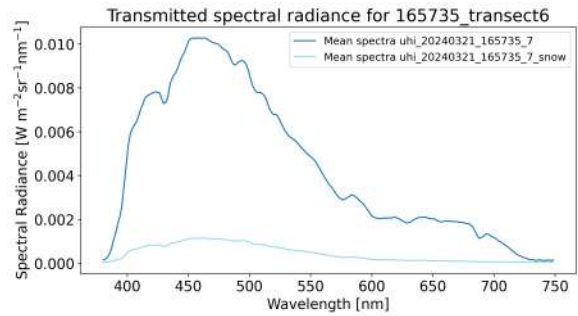


Figure 4.13.d: Transmitted spectral radiance through bare (dark blue) and snow-covered (light blue) ice for flight 6.

Figure 4.13: Mean incoming and transmitted spectral radiance plots for flight 4 (4.13.a, 4.13.b) and 6 (4.13.c, 4.13.d). Note the different y-axis scales between the four figures.

For a better comparison between the spectral signatures of the transmitted radiance under bare ice and snow-covered ice, we normalize the spectra for both flights, as shown in Figure 4.14. As can be seen, the spectral signatures are nearly identical, indicating that snow and ice attenuate similar wavelengths of light.

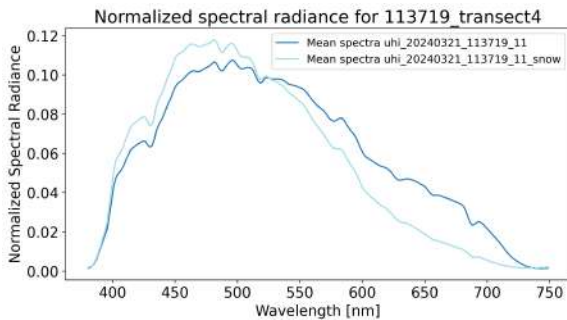


Figure 4.14.a: Normalized under-ice spectral radiance for flight 4.

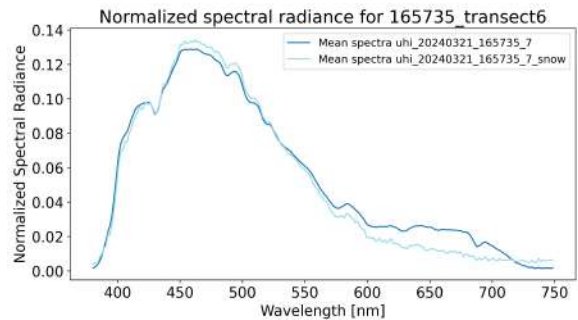


Figure 4.14.b: Normalized under-ice spectral radiance for flight 6.

Figure 4.14: Normalized under-ice spectral radiance for flight 4 (left) and flight 6 (right). The normalization highlights the similar spectral signature of the bare and snow-covered ice, and between midday and early evening.

We obtained the spectral incoming irradiance by applying (2.2) from Section 2.2. The results are illustrated in Figure 4.15.a for run 4 and 4.15.c for run 6.

We calculate the transmitted spectral irradiance using (3.3), as presented by Katlein, Nicolaus, and Petrich in [15], with conversion coefficient values of  $C$  set to  $\pi$ , 2.5, 1.68, and 1.3. For  $C = \pi$ , (3.3)

is equivalent to (2.4), which is the most widely used conversion in current research, and serves as our baseline reference. As indicated by (3.3), when  $C = 2.5$ , the anisotropic scattering coefficient is zero, meaning this scenario assumes isotropic scattering through ice. Values near 2.5 are typically observed in granular ice, while columnar ice generally exhibits smaller values between 1.3 and 2.3 [15]. The median  $C$  value reported in [15] across multiple experiments is  $C = 1.68$ , while  $C = 1.3$  is the modelled value used by the authors. For our analysis, we adopt these latter two values, since we do not have specific anisotropic scattering coefficients from our fieldwork. The  $C$  values, corresponding anisotropic scattering coefficients  $\gamma$ , and the scattering types are summarized in Table 4.5.

<b>C Value</b>	$\gamma$	<b>Scattering Type</b>
$\pi$	N/A	isotropic
2.5	0	isotropic
1.68	0.41	anisotropic
1.3	0.6	anisotropic

Table 4.5:  $C$  values and their corresponding anisotropic scattering coefficients used for the conversion from spectral radiance to spectral irradiance. The scattering type indicates whether the value assumes isotropic or anisotropic scattering through sea ice.

The calculated spectral irradiance for each  $C$  value is plotted in Figure 4.15.b for flight 4 and 4.15.d for flight 6. Note the different y-axis scales, especially between Figures 4.15.b and 4.15.d. The transmitted spectral irradiance is more than one order of magnitude higher in the fourth run than in the sixth.

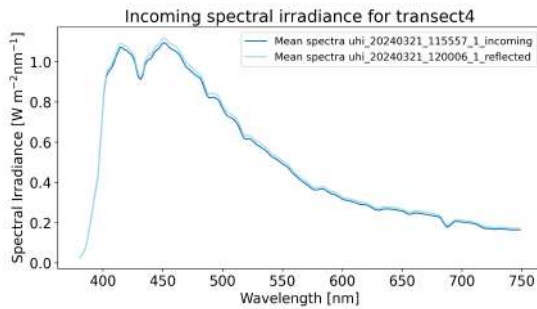


Figure 4.15.a: Incoming spectral irradiance

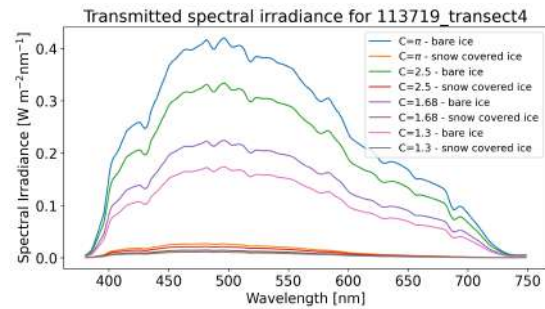


Figure 4.15.b: Under-ice transmitted spectral irradiance

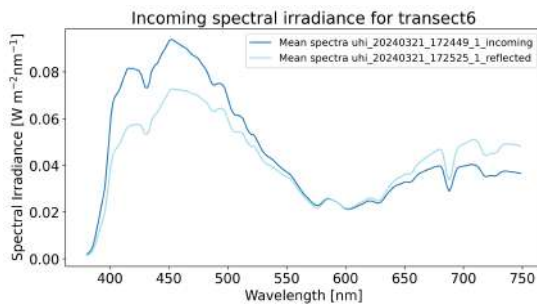


Figure 4.15.c: Incoming spectral irradiance

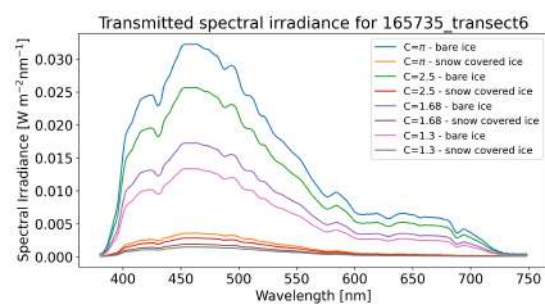


Figure 4.15.d: Under-ice transmitted spectral irradiance

Figure 4.15: Incoming and transmitted spectral irradiance plots for flights 4 and 6. Note that for the incoming irradiance plots (Figures 4.15.a and 4.15.c) the y-axis values are scaled by a factor of  $\pi$  when compared to the Figures 4.13.a and 4.13.c. The plots in Figures 4.15.b and 4.15.d show the transmitted irradiance measurements for each of the four  $C$  values, and correspond to the transmitted radiance measurements in Figures 4.13.b and 4.13.d.

In addition to the spectral radiance and irradiance, we analysed the integrated incoming and transmitted irradiance. The results are summarized in Table 4.6. The integrated irradiance under bare ice at sunset decreased to approximately 5% of the transmitted irradiance measured earlier in the day, while

under snow-covered ice about 10% remained. For bare ice, the largest decrease occurred in the red wavelengths. Under snow-covered ice, the red and green wavelengths showed similar decreases from midday to evening. In the blue wavelengths, 7.7% of the light transmitted during flight 4 remained during flight 6 under bare ice, compared to 13.1% under snow-covered ice.

When comparing the incoming and reflected light, the reflected irradiance is slightly lower for all measurements, except the red wavelengths during run 6. This is consistent with the spectral radiance and irradiance plots (Figures 4.13 and 4.15). Additionally, the intensity of the incoming red wavelengths at sunset is reduced to approximately 15% of the midday levels, while for reflected light, it is almost 20%. The increase in red wavelengths can be explained by the reduced scattering efficiency of red light in the atmosphere [49].

<b>Transmitted Irradiance [<math>W m^{-2}</math>]</b>					
<b>Wavelengths</b>	<b>C</b>	<b>Bare - F4</b>	<b>Bare - F6</b>	<b>Snow - F4</b>	<b>Snow - F6</b>
All (380-750 nm)	$\pi$	86.4473	5.0376	4.6470	0.5079
Red (620-750 nm)	$\pi$	13.1326	0.5087	0.3222	0.0317
Green (495-570 nm)	$\pi$	27.7431	1.3973	1.5916	0.1486
Blue (450-495 nm)	$\pi$	17.2459	1.3404	1.1303	0.1482
All (380-750 nm)	2.5	68.7926	4.0088	3.6980	0.4042
Red (620-750 nm)	2.5	10.4506	0.4048	0.2564	0.0252
Green (495-570 nm)	2.5	22.0773	1.1119	1.2666	0.1183
Blue (450-495 nm)	2.5	13.7239	1.0666	0.8995	0.1180
All (380-750 nm)	1.68	46.2286	2.6939	2.4850	0.2716
Red (620-750 nm)	1.68	7.0228	0.2720	0.1723	0.0170
Green (495-570 nm)	1.68	14.8359	0.7472	0.8511	0.0795
Blue (450-495 nm)	1.68	9.2224	0.7168	0.6045	0.0793
All (380-750 nm)	1.3	35.7721	2.0846	1.9229	0.2102
Red (620-750 nm)	1.3	5.4343	0.2105	0.1333	0.0131
Green (495-570 nm)	1.3	11.4802	0.5782	0.6586	0.0615
Blue (450-495 nm)	1.3	7.1364	0.5546	0.4677	0.0613
<b>Incoming and Reflected Irradiance [<math>W m^{-2}</math>]</b>					
<b>Wavelengths</b>	<b>C</b>	<b>Incoming -F4</b>	<b>Incoming -F6</b>	<b>Reflected- F4</b>	<b>Reflected- F6</b>
All (380-750 nm)	$\pi$	191.5565	17.2951	186.7274	15.875476
Red (620-750 nm)	$\pi$	28.8079	4.4323	27.6158	5.2912
Green (495-570 nm)	$\pi$	43.9277	3.4635	42.7934	3.1541
Blue (450-495 nm)	$\pi$	42.5482	3.6863	41.6357	2.9878

Table 4.6: Comparison of mean total irradiance measurements for different wavelengths and different  $C$  values for flight 4 (F4) and flight 6 (F6).

### 4.2.3 Radiative Transfer Models

We applied the radiative transfer models (2.7) and (3.3), from Perovich [11] and Nicolaus and Katlein [24], respectively, to calculate the spectral extinction coefficients of sea ice based on the transmitted irradiance derived using each of the four  $C$  values. In the absence of direct albedo measurements, we used the Two-streAm Radiative TransfEr in Snow (TARTES) model [50] to obtain plausible spectral albedos, accounting for the specific snow and ice conditions, including snow density ( $248 kg/m^3$ ), a solar zenith sun angle of  $77^\circ$  for flight 4, and diffuse light scattering typical near sunset for flight 6. The calculated total albedos are 0.91 and 0.86 for snow, and 0.55 and 0.48 for bare ice, for the afternoon and evening, respectively. The albedo values coincide with previous values observed in the Arctic [11, 17, 22]. The bare ice albedo values are lower than those taken mid-summer by Light et al [12], which is

to be expected, due to the higher sun angle in June and July. The model by Nicolaus and Katlein is a simplified version of the Perovich model, and neglects the influence of albedo.

To calculate the spectral extinction coefficients of the snow, we adapted the models to a two-layer system. For (2.7) this becomes:

$$E(\lambda) = (1 - \alpha_\lambda)E_0(\lambda)e^{-\kappa_{\lambda s}z_s}e^{-\kappa_{\lambda i}z_i} \quad (4.4)$$

where  $\kappa_{\lambda s}$  and  $\kappa_{\lambda i}$  are the extinction coefficients for snow and ice respectively,  $z_s$  is the snow depth, and  $z_i$  is the ice thickness. Rearranging for  $\kappa_{\lambda s}$  the equation becomes:

$$\kappa_{\lambda s} = \frac{-1}{z_s} \left[ \ln \left( \frac{E(\lambda)}{E_0(\lambda) * (1 - \alpha_\lambda)} \right) + \kappa_{\lambda i}z_i \right] \quad (4.5)$$

where  $\alpha_\lambda$  is the spectral snow albedo calculated using the TARTES model. This gives the spectral extinction coefficients for the Perovich model. For the Nicolaus and Katlein model this equation simplifies to:

$$\kappa_{\lambda s} = \frac{-1}{z_s} \left[ \ln \left( \frac{E(\lambda)}{E_0(\lambda)} \right) + \kappa_{\lambda i}z_i \right] \quad (4.6)$$

The results of the two models are presented in the following chapter.

# Chapter 5

## Results

This chapter presents the results of the radiative transfer models and corresponding ice thickness estimates. Additionally, we calculate ice thickness using Stefan's Law. In the final section, we visualize the spectral transmittance through both bare and snow-covered ice, obtained during the field work. These results are compared and discussed in Chapter 6.

### 5.1 Radiative Transfer Models - Spectral Extinction Coefficients

To determine the spectral extinction coefficients, we applied the radiative transfer models from Perovich [11] and from Nicolaus and Katlein [24] to the transmitted spectral irradiance calculated in Section 4.2.2. Specifically, the Perovich model uses (2.7) and (4.5), and the Nicolaus and Katlein model uses (3.3) and (4.6), each for ice and snow, respectively. We used the average measured thicknesses of  $0.22\text{ m}$  for snow and  $0.65\text{ m}$  for ice. To smooth the data and reduce noise, we applied a Savitzky-Golay filter and omitted wavelengths outside the  $400\text{-}705\text{ nm}$  range. The resulting spectral extinction coefficients are visualized in Figure 5.1.

For snow, the spectral extinction coefficients remain the same across all  $C$  values listed in Table 4.5, and so only a single curve is shown for each model. For bare ice, there is some variation among the different conversion factors. These variances, as well as differences between the results from flight 4 (Figure 5.1.a) and flight 6 (Figure 5.1.b) are addressed in Chapter 6.

A red dotted line in Figures 5.1.a and 5.1.b is drawn at  $y = 0$ , highlighting that the Perovich model outputs negative extinction coefficients in the green to red wavelengths for flight 4 when isotropic scattering is assumed (*i.e.*  $C = \pi$  and  $C = 2.5$ ). Negative extinction coefficients are invalid, and these results are also discussed in Chapter 6.

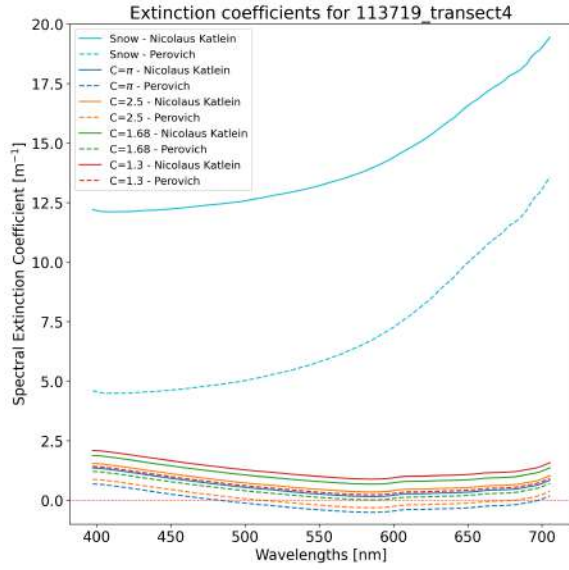


Figure 5.1.a: Extinction coefficients for flight 4.

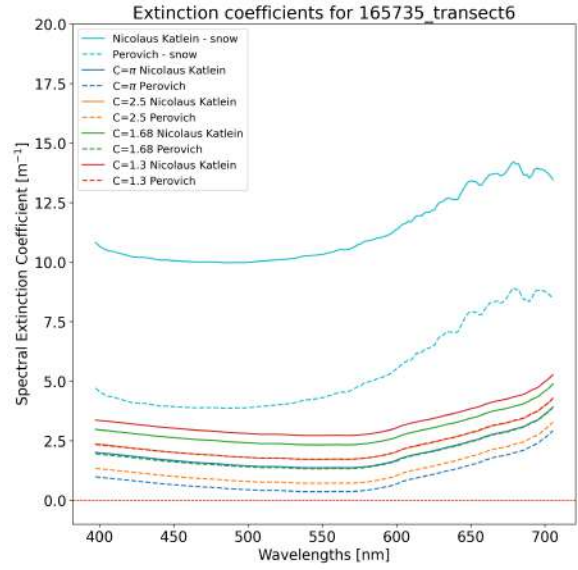


Figure 5.1.b: Extinction coefficients for flight 6.

Figure 5.1: Spectral extinction coefficients for flight 4 (*left*) and flight 6 (*right*) calculated using the models by Perovich [11] and Nicolaus and Katlein [24]. The red dotted line marks  $y = 0$ .

## 5.2 Estimating Ice Thickness Using Radiative Transfer Models

To estimate ice thickness, we modelled the transmitted spectral irradiance under snow-covered ice, using the calculated extinction coefficients. The radiative transfer model presented by Perovich [11] applies (4.4), while the Nicolaus and Katlein model omits the  $(1 - \alpha_\lambda)$  term, resulting in a slightly simplified model:

$$E_m(\lambda) = E_0(\lambda)e^{-\kappa_{\lambda s}z_s}e^{-\kappa_{\lambda i}z_i} \quad (5.1)$$

Each model was run across a range of plausible snow depths and ice thicknesses. For the Perovich model we used  $N = 300$  values from 0.1-1.1  $m$  for snow depth, and from 0.1-2.0  $m$  for ice thickness. For the Nicolaus and Katlein model we reduced the upper bound for snow depth to 0.6  $m$ . The bounds, also displayed on the  $x$  and  $y$  axes of the plots in Figures 5.2 - 5.9, were chosen based on empirical testing and practical constraints.

To evaluate model performance, we minimized the Mean Relative Error (MRE) between the modelled and measured transmitted spectral irradiance, optimizing for snow and ice thickness:

$$\text{MRE} = \frac{1}{N} \sum \left( \frac{|E(\lambda) - E_m(\lambda)|}{|E(\lambda)|} \right) \quad (5.2)$$

Here,  $E_m(\lambda)$  is the modelled, and  $E(\lambda)$  the measured transmitted spectral irradiance. This analysis was repeated for each set of extinction coefficients, resulting in four estimation plots per model per run. Results for the Perovich model are shown in Figures 5.2 and 5.4 for flights 4 and 6, respectively. Results for the Nicolaus and Katlein model are visualized in Figures 5.3 and 5.5, again for flights 4 and 6, respectively. For each optimization, the results with a mean relative error less than 0.1 are outlined in red, and results with an error less than 0.5 are outlined in orange. While the results are presented here,

key differences are highlighted and analysed in Chapter 6.

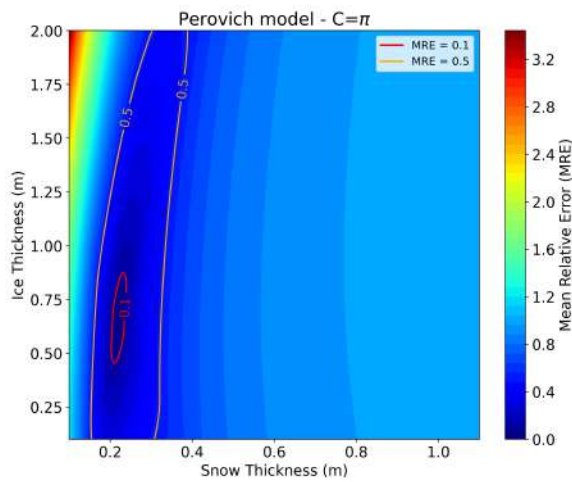


Figure 5.2.a:  $C = \pi$ .

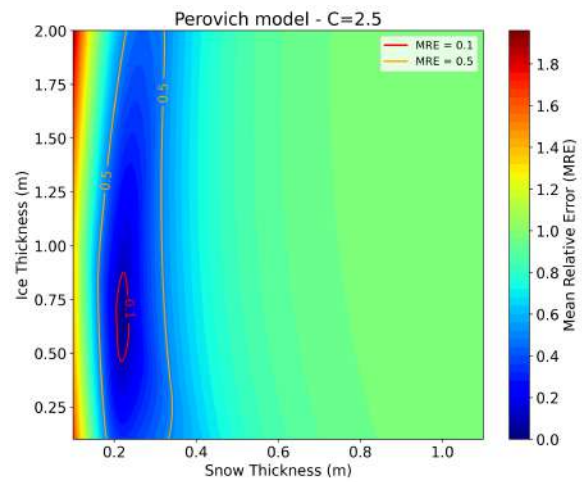


Figure 5.2.b:  $C = 2.5$ .

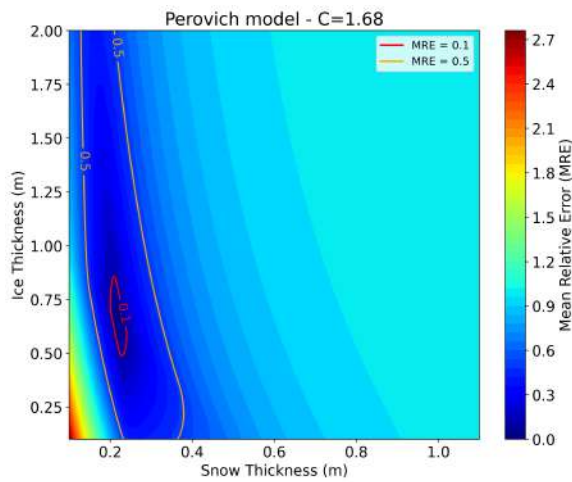


Figure 5.2.c:  $C = 1.68$ .

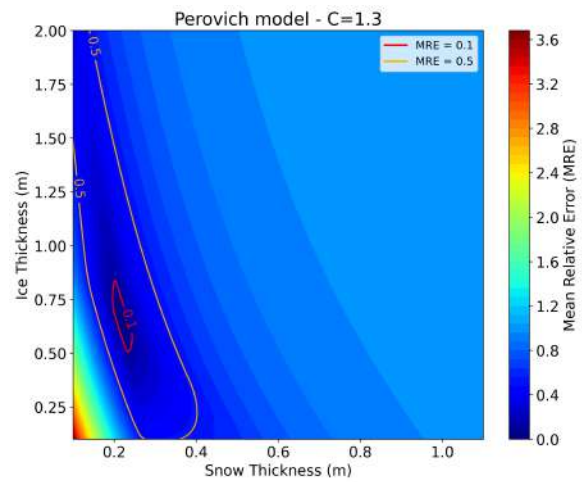


Figure 5.2.d:  $C = 1.3$ .

Figure 5.2: Optimized snow depth and ice thickness estimations from flight 4 data using the Perovich model. Estimates were computed using the spectral transmitted irradiance calculated using  $C = \pi$  (5.2.a),  $C = 2.5$  (5.2.b),  $C = 1.68$  (5.2.c), and  $C = 1.3$  (5.2.d). The mean relative error boundaries for 0.1 and 0.5 are shown in red and orange, respectively.

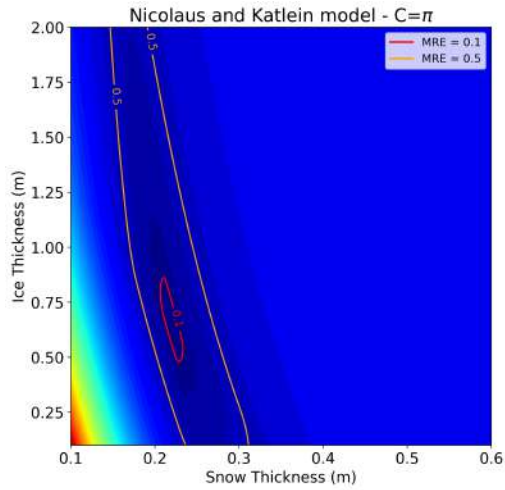


Figure 5.3.a:  $C = \pi$ .

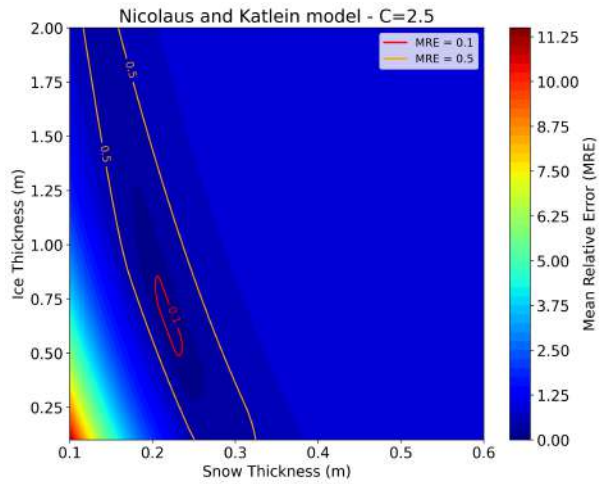


Figure 5.3.b:  $C = 2.5$ .

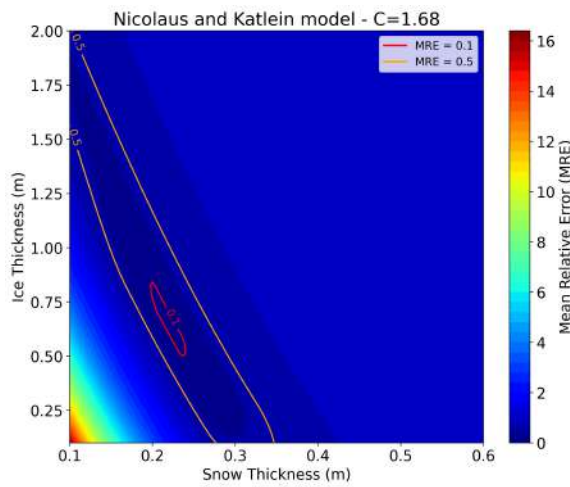


Figure 5.3.c:  $C = 1.68$ .

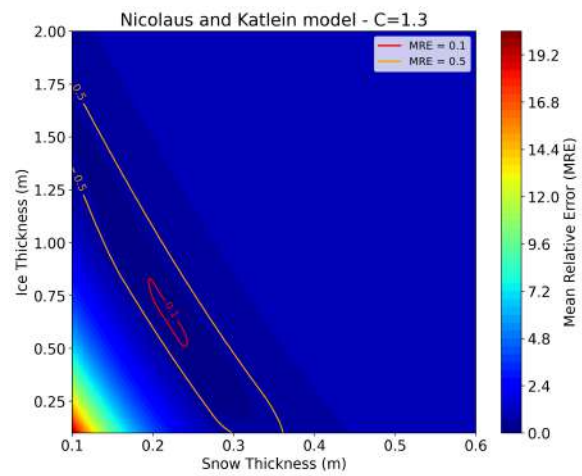


Figure 5.3.d:  $C = 1.3$ .

Figure 5.3: Optimized snow depth and ice thickness estimations from flight 4 data using the Nicolaus and Katlein model. Estimates were computed using the spectral transmitted irradiance calculated using  $C = \pi$  (5.3.a),  $C = 2.5$  (5.3.b),  $C = 1.68$  (5.3.c), and  $C = 1.3$  (5.3.d). The mean relative error boundaries of 0.1 and 0.5 are shown in red and orange, respectively.

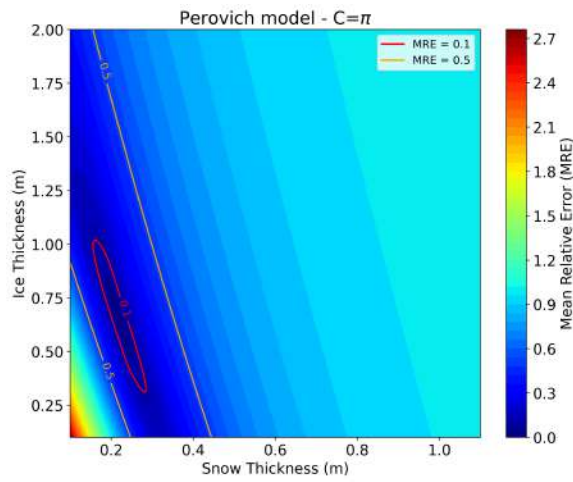


Figure 5.4.a:  $C = \pi$ .

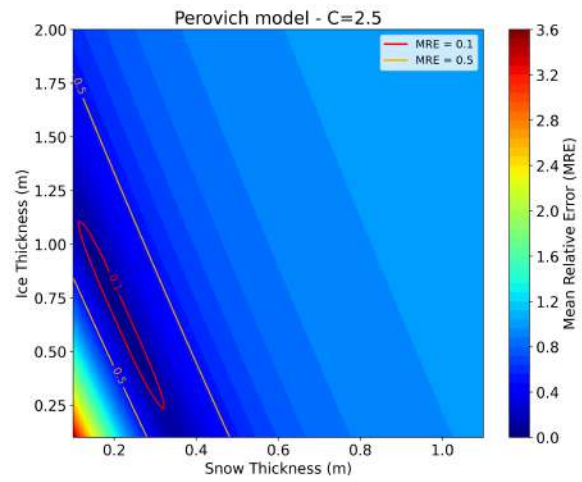


Figure 5.4.b:  $C = 2.5$ .

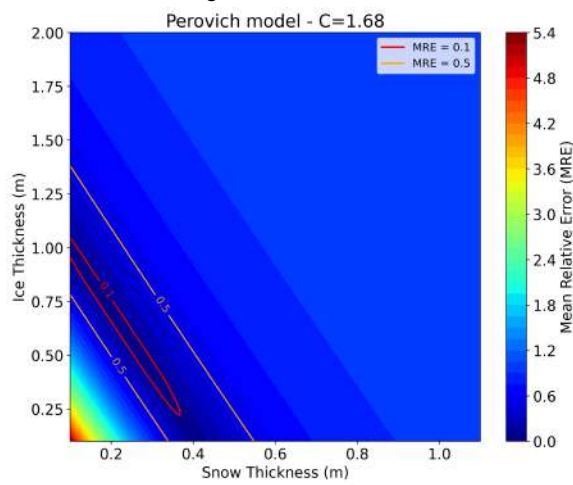


Figure 5.4.c:  $C = 1.68$ .

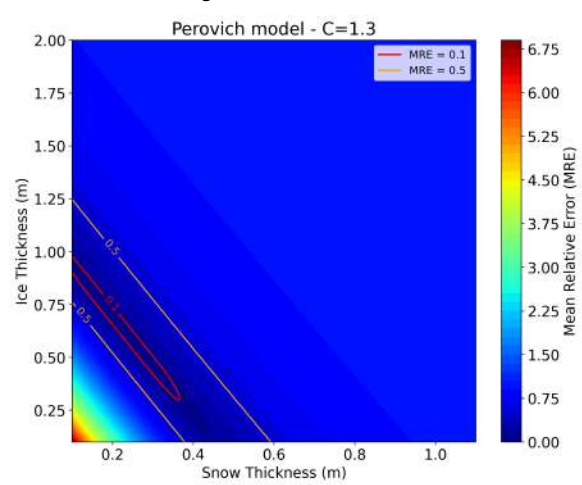


Figure 5.4.d:  $C = 1.3$ .

Figure 5.4: Optimized snow and ice thickness from flight 6 data using the Perovich model. Estimates were computed using the spectral transmitted irradiance calculated using  $C = \pi$  (5.4.a),  $C = 2.5$  (5.4.b),  $C = 1.68$  (5.4.c), and  $C = 1.3$  (5.4.d). The mean relative error boundaries for 0.1 and 0.5 are shown in red and orange, respectively.

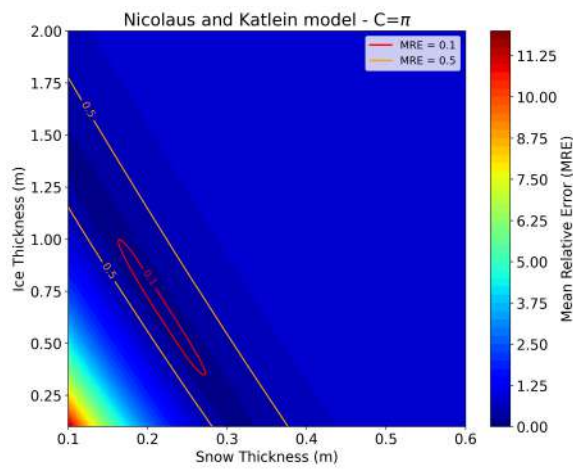


Figure 5.5.a:  $C = \pi$ .

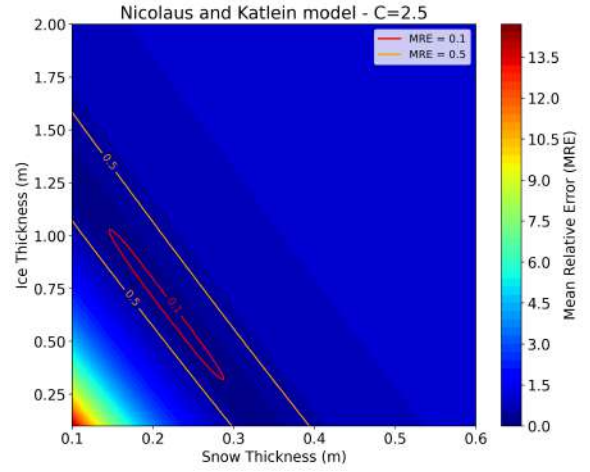


Figure 5.5.b:  $C = 2.5$ .

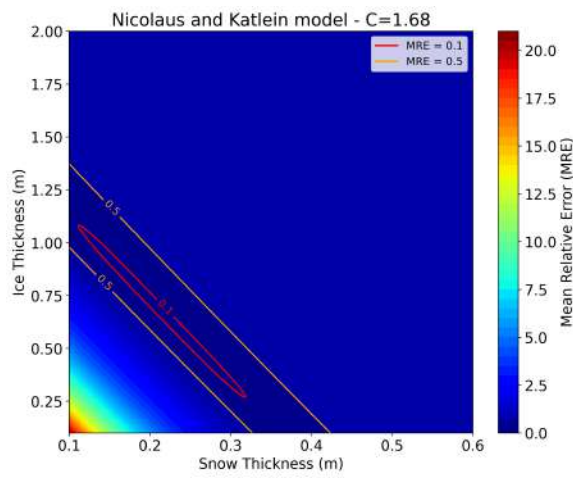


Figure 5.5.c:  $C = 1.68$ .

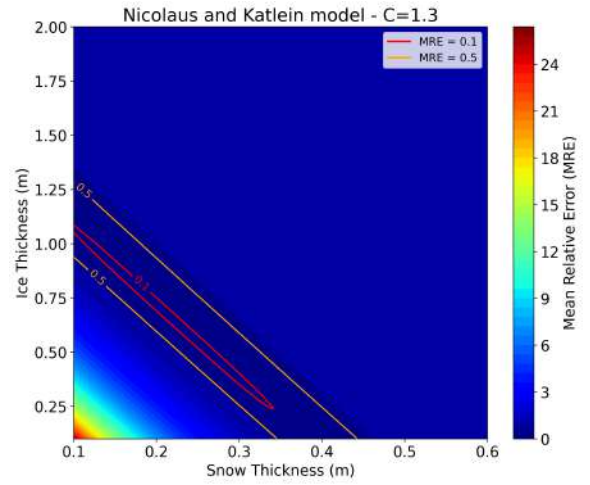


Figure 5.5.d:  $C = 1.3$ .

Figure 5.5: Optimized snow and ice thickness from flight 6 data using the Nicolaus and Katlein model. Estimates were computed using the spectral transmitted irradiance calculated using  $C = \pi$  (5.5.a),  $C = 2.5$  (5.5.b),  $C = 1.68$  (5.5.c), and  $C = 1.3$  (5.5.d). The mean relative error boundaries of 0.1 and 0.5 are shown in red and orange, respectively.

The above results, (Figures 5.2 through 5.5), all assume the same scattering properties through bare ice and snow-covered ice. However, since scattering in snow is isotropic, while sea ice scattering is largely anisotropic [15], this does not accurately reflect the real world. To address this inconsistency, we apply the models again with conversion factors  $C_s = \pi$  and  $C_s = 2.5$  for the snow-covered ice (corresponding to isotropic scattering), since snow dominates the light absorption in this case, and  $C_i = 1.68$  and  $C_i = 1.3$  for bare ice (corresponding to anisotropic scattering coefficients). This greatly improves the results for the Perovich model, shown in Figures 5.6 and 5.8 for flights 4 and 6, respectively. The Nicolaus and Katlein model only improves slightly, as shown in Figures 5.7 and 5.9 for flights 4 and 6.

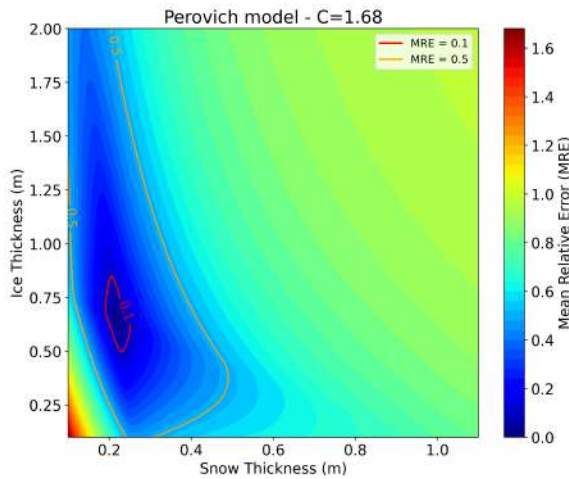


Figure 5.6.a:  $C_i = 1.68$ ;  $C_s = \pi$ .

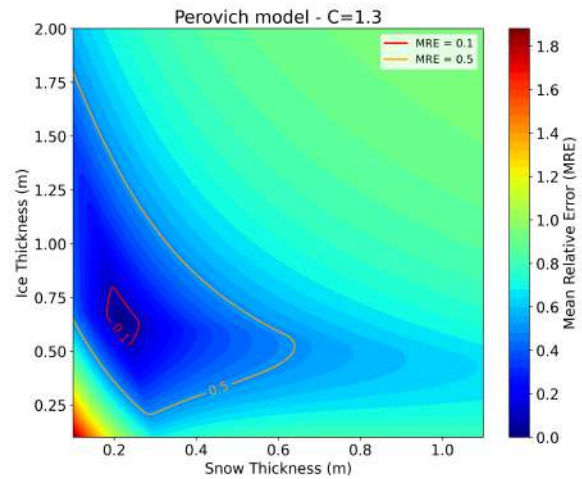


Figure 5.6.b:  $C_i = 1.3$ ;  $C_s = \pi$ .

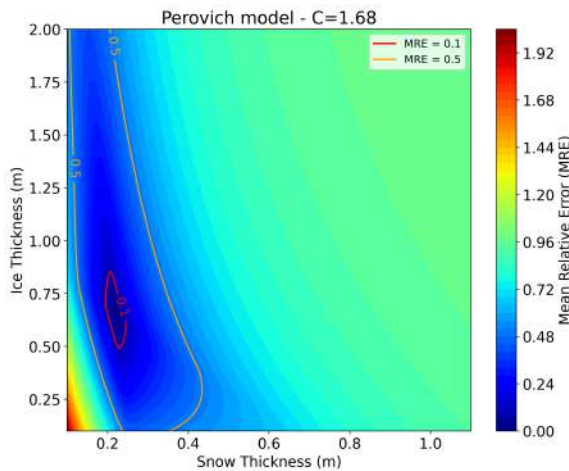


Figure 5.6.c:  $C_i = 1.68$ ;  $C_s = 2.5$ .

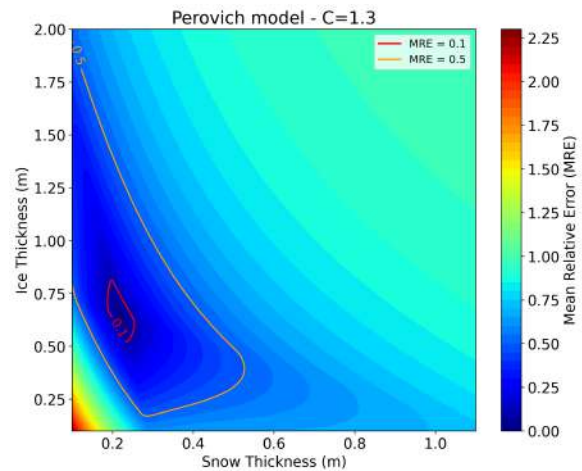


Figure 5.6.d:  $C_i = 1.3$ ;  $C_s = 2.5$ .

Figure 5.6: Optimized snow and ice thickness from flight 4 data using the Perovich model. Estimates were computed using the spectral transmitted irradiance calculated considering anisotropic scattering for bare ice and isotropic scattering for snow-covered ice. The mean relative error boundaries of 0.1 and 0.5 are shown in red and orange, respectively.

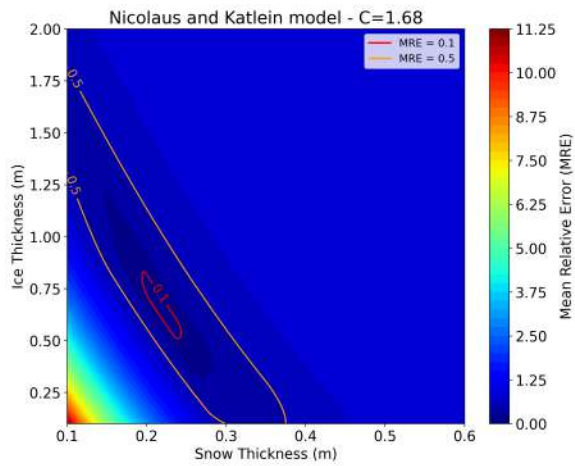


Figure 5.7.a:  $C_i = 1.68$ ;  $C_s = \pi$ .

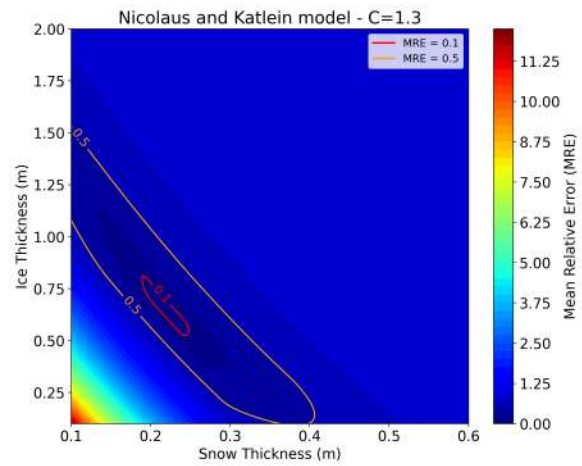


Figure 5.7.b:  $C_i = 1.3$ ;  $C_s = \pi$ .

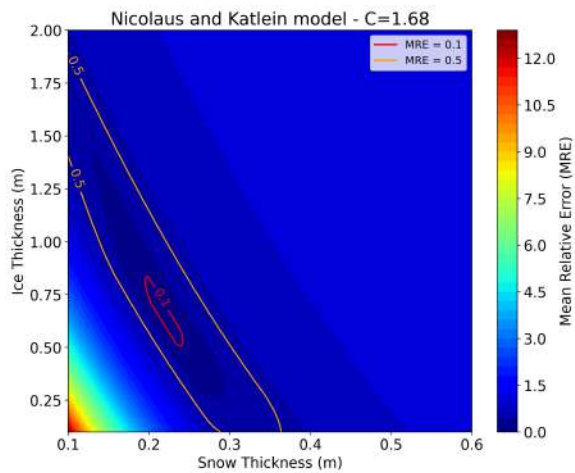


Figure 5.7.c:  $C_i = 1.68$ ;  $C_s = 2.5$ .

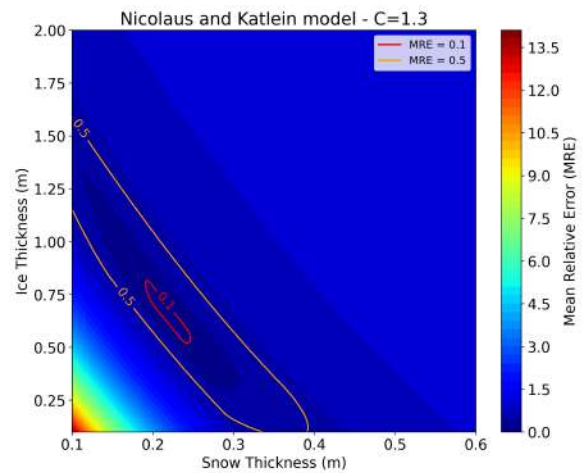


Figure 5.7.d:  $C_i = 1.3$ ;  $C_s = 2.5$ .

Figure 5.7: Optimized snow and ice thickness from flight 4 data using the Nicolaus and Katlein model. Estimates were computed using the spectral transmitted irradiance calculated considering anisotropic scattering for bare ice and isotropic scattering for snow-covered ice. The mean relative error boundaries of 0.1 and 0.5 are shown in red and orange, respectively.

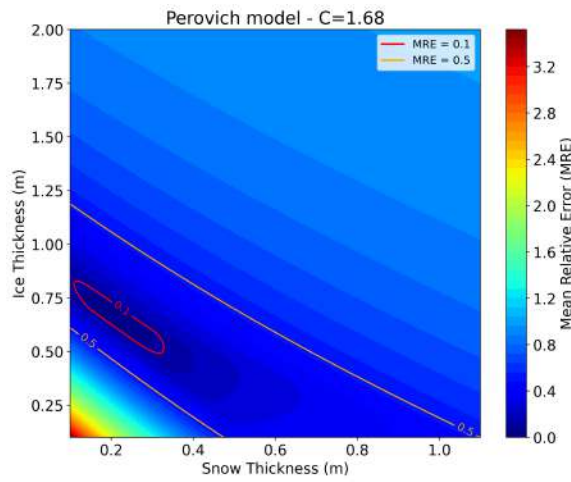


Figure 5.8.a:  $C_i = 1.68$ ;  $C_s = \pi$ .

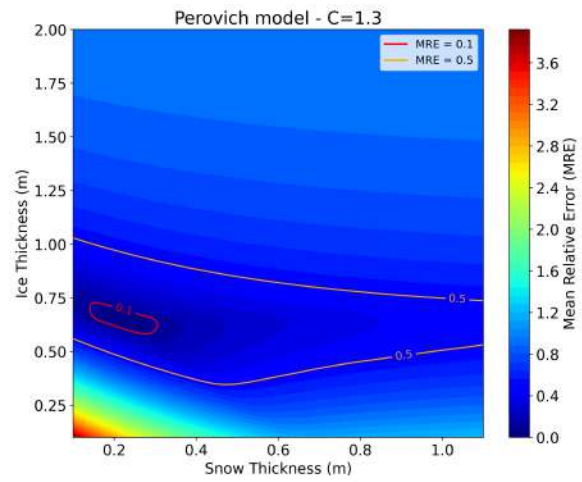


Figure 5.8.b:  $C_i = 1.3$ ;  $C_s = \pi$ .

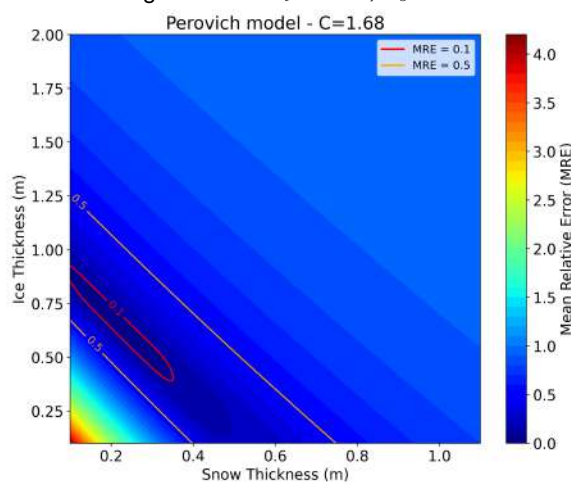


Figure 5.8.c:  $C_i = 1.68$ ;  $C_s = 2.5$ .

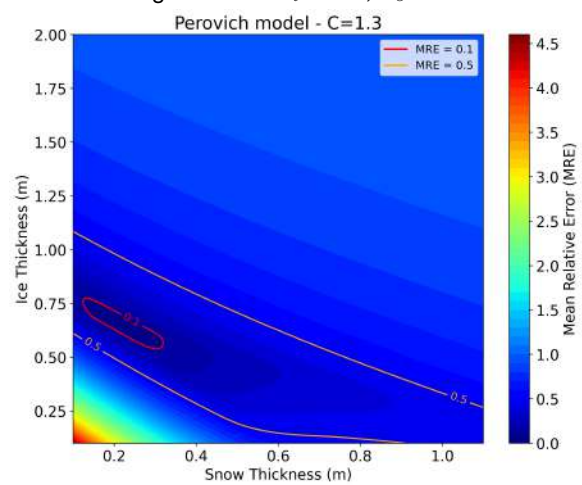


Figure 5.8.d:  $C_i = 1.3$ ;  $C_s = 2.5$ .

Figure 5.8: Optimized snow and ice thickness from flight 6 data using the Perovich model. Estimates were computed using the spectral transmitted irradiance calculated considering anisotropic scattering for bare ice and isotropic scattering for snow-covered ice. The mean relative error boundaries of 0.1 and 0.5 are shown in red and orange, respectively.

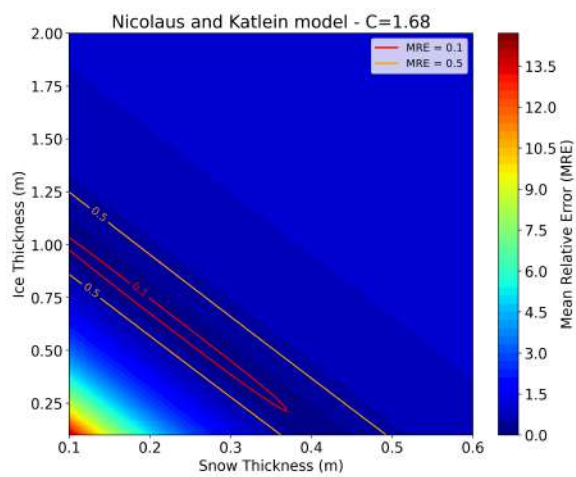


Figure 5.9.a:  $C_i = 1.68$ ;  $C_s = \pi$ .

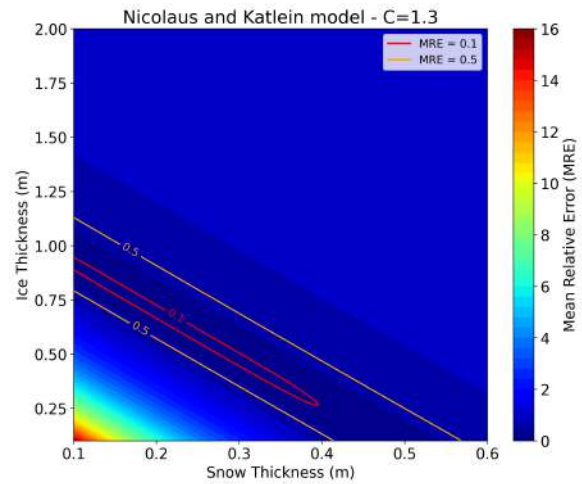


Figure 5.9.b:  $C_i = 1.3$ ;  $C_s = \pi$ .

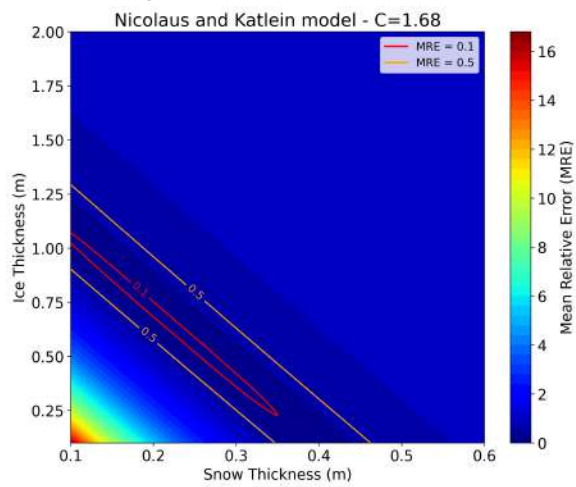


Figure 5.9.c:  $C_i = 1.68$ ;  $C_s = 2.5$ .

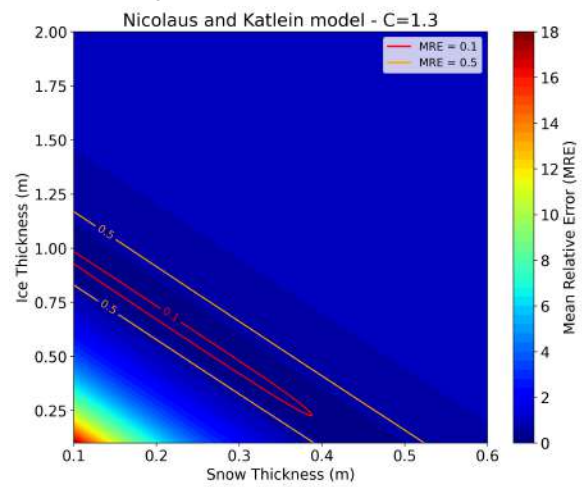


Figure 5.9.d:  $C_i = 1.3$ ;  $C_s = 2.5$ .

Figure 5.9: Optimized snow and ice thickness from flight 6 data using the Nicolaus and Katlein model. Estimates were computed using the spectral transmitted irradiance calculated considering anisotropic scattering for bare ice and isotropic scattering for snow-covered ice. The mean relative error boundaries of 0.1 and 0.5 are shown in red and orange, respectively.

### 5.3 Estimating Ice Thickness Using Stefan’s Law

Using measurements from Akseløya Weather Station, located at the mouth of Van Mijenfjorden, we calculated the FDD for the winter season from 2023 to 2024. At the time of our fieldwork FDD was equal to -1215. The mean daily temperatures are visualized in Figure 5.10.

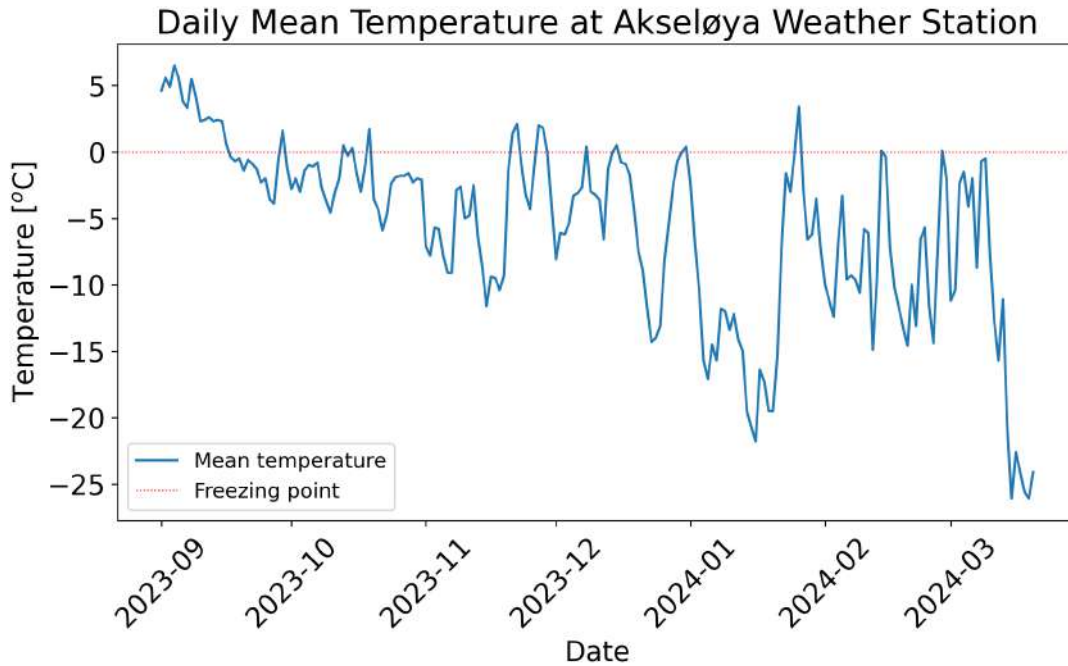


Figure 5.10: Freezing degree days at Akseløya Weather Station [51].

Additionally, we used the parameters in Table 5.1 to calculate the expected ice thickness according to Stefan’s Law (2.2). Initial ice thickness is 0, since we are dealing with first year ice. The values for snow thickness and ice density are averaged from the measurements taken by other students during the field excursion. The thermal conductivity of snow is the average value used in the modelling community [52]. The thermal conductivity of ice is adapted from the values in [53].

The two solutions to the quadratic equation (2.2) are 0.64 m or 2.16 m. We discard 2.16 m as a possible solution, since we know the ice cannot be this thick, and are left with an estimated ice thickness of 0.64 m. This matches the measurements taken in the field, showing that Stefan’s Law holds, and thus can be used as ground truth for the ice thickness if no *in situ* measurements are available.

Parameter	Symbol	Value	Unit
Initial ice thickness	$h_{i0}$	0	m
Snow thickness	$h_s$	0.22	m
Thermal conductivity of ice	$k_i$	2.1	W/m·K
Thermal conductivity of snow	$k_s$	0.33	W/m·K
Density of ice	$\rho_i$	953.7	kg/m <sup>3</sup>
Latent heat of fusion for ice	$l_i$	$3.33 \times 10^5$	J/kg
Correction factor	$\alpha$	86400	-

Table 5.1: Stefan’s Law parameters with their corresponding units.

## 5.4 Spectral Transmittance

Using the incoming and transmitted spectral irradiance calculated in Section 4.2.2, we plot the light transmittance through the ice for each  $C$  value for bare ice and snow-covered ice. The results are shown in Figure 5.11. For run 4 the transmittance through snow-covered ice (Figure 5.11.b) is approximately 5% of the transmittance through bare ice (Figure 5.11.a). For run 6 this is significantly higher, with transmittance through snow-covered ice (Figure 5.11.d) at approximately 10-12% of bare ice (Figure 5.11.c). Overall, the transmittance through bare ice decreases by about half between the afternoon and evening, while it stays relatively constant through snow-covered ice. The factors contributing to these variations are explored in Chapter 6.

The corresponding total transmittance values are summarized in Table 5.2.

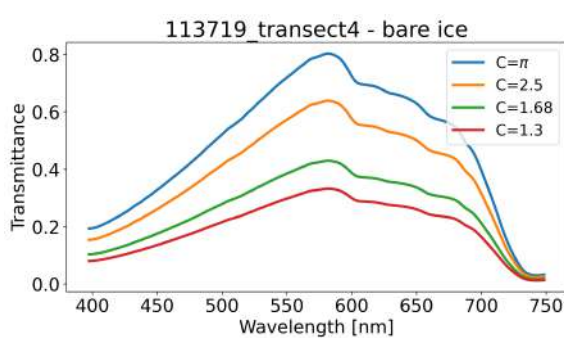


Figure 5.11.a: Transmittance through bare ice during flight 4.

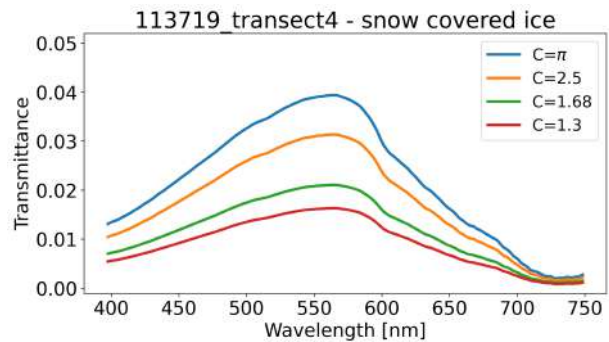


Figure 5.11.b: Transmittance through snow-covered ice during flight 4.

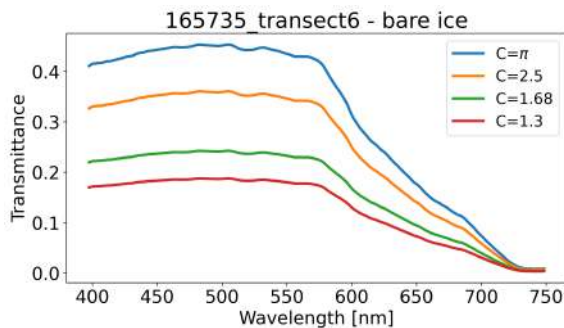


Figure 5.11.c: Transmittance through bare ice during flight 6.

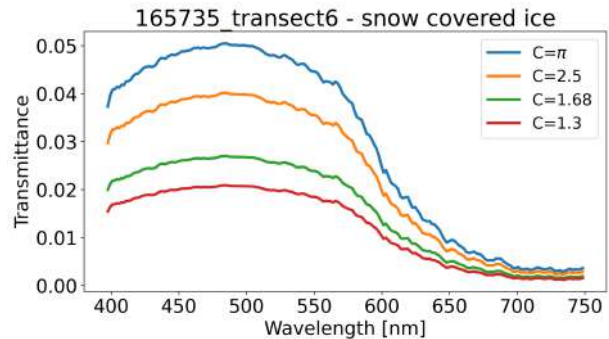


Figure 5.11.d: Transmittance through snow-covered ice during flight 6.

Figure 5.11: Spectral transmittance calculated for bare ice (left) and snow-covered ice (right) for flights 4 (*top*) and 6 (*bottom*). Note the change in y-axis scale between the bare ice transmittance for the two flights.

$C$	Bare - F4	Bare - F6	Snow-covered - F4	Snow-covered - F6
$\pi$	$0.46 \pm 0.20$	$0.32 \pm 0.17$	$0.02 \pm 0.01$	$0.03 \pm 0.02$
2.5	$0.36 \pm 0.16$	$0.25 \pm 0.13$	$0.02 \pm 0.01$	$0.03 \pm 0.02$
1.68	$0.24 \pm 0.10$	$0.17 \pm 0.09$	$0.01 \pm 0.01$	$0.02 \pm 0.01$
1.3	$0.19 \pm 0.08$	$0.13 \pm 0.07$	$0.01 \pm 0.00$	$0.01 \pm 0.01$

Table 5.2: Total transmittance and standard deviation through bare and snow-covered ice.

# Chapter 6

## Discussion

In this chapter we provide an interpretation of the results presented in the previous section, and a comparison to previous works. Additionally, we address some limitations of the approaches of this study.

### 6.1 Radiative Transfer Models - Spectral Extinction Coefficients

To evaluate the radiative transfer models, we begin by looking at the calculated spectral extinction coefficients, and compare them to previous studies.

For snow, the calculated coefficients vary greatly between the two models: the Nicolaus and Katlein approach outputs much higher coefficients than the model presented by Perovich. For bare ice, the difference between the models is much less pronounced, but the same trend is still apparent. The two flights output similar results, with the data from the sixth run giving slightly lower coefficients. For run 4, the spectral extinction coefficients dip below zero for wavelengths 500-700 *nm* when calculated with the Perovich model and assuming isotropic scattering through sea ice. Negative extinction coefficients would imply that the light intensity increases as it travels through the sea ice, contradicting the physical principle that absorption and scattering cause light to lose intensity when passing through a medium. Thus, we can regard these extinction coefficients as invalid results.

Our results for snow compare well with the spectral extinction coefficients outlined in the two subfigures in Figure 3.4. The spectral extinction coefficients calculated for snow using the Nicolaus and Katlein model match nicely with Figure 3.4.a. The Perovich model for snow matches more closely with the dry snow coefficients in Figure 3.4.b.

For bare ice, our extinction coefficients calculated using the Nicolaus and Katlein model are generally higher than those seen in Figures 3.4.a and 3.4.b. Our values all lie above 1, while those in previous studies fall in the range between 0.1 and 1 [11, 12]. The coefficients calculated using the Perovich model are slightly lower, and match the values in these studies more closely. The spectral shapes are also comparable, with our values showing less of an increase in the red wavelengths than those seen in previous studies [11, 12, 22].

## 6.2 Ice Thickness Estimation

To analyse the optimized snow and ice thicknesses estimated in Chapter 5 we compare results between the Perovich and the Nicolaus and Katlein models, and between flights 4 and 6. For each optimization plot shown in Figures 5.2 through 5.9, we use the mean relative errors less than 0.1 and 0.5 to evaluate the performance of the model. We compare the results with the ground truth data shown in Table 4.4.

For each optimization, the results with a mean relative error less than 0.1 and 0.5 are outlined in red and orange, respectively. For both models and both flights, the ice thickness estimated with an error value of less than 0.5 ranges quite significantly, admitting all thicknesses between 0-2  $m$  for both models for run 4 (Figures 5.2 and 5.6 for the Perovich model, and 5.3 and 5.7 for Nicolaus and Katlein). In certain cases, this 2  $m$  span is reached even for a single snow depth (Figures 5.2.a, 5.2.b). For run 6 the upper bound of this range decreases with the  $C$  values, with a maximum still at 2  $m$  for  $C = \pi$  (Figure 5.4.a) and a smallest upper bound just above 1  $m$  when  $C_i = 1.3$  through ice and  $C_s = \pi$  through snow (Figure 5.8.b).

The snow depth range is limited in comparison, with the evaluations reaching a maximum span of approximately 0.15  $m$  for a single ice thickness for the Nicolaus and Katlein model (Figures 5.9.a and 5.9.b). The Perovich models admit a larger range of snow depths within the 0.5 error bound, with the maximum range being more than 1  $m$  for a single ice thickness (Figure 5.8.b). Knowing that snow has a much higher effect than ice thickness on light attenuation, the higher distribution in ice thicknesses compared to snow depth is to be expected.

The upper bound of the anisotropic  $C$  values is the same between the two models for flight 6 when the same scattering coefficient is considered through ice and snow. For  $C = 1.68$  this lies around 1.3  $m$  (Figures 5.4.c), and for  $C = 1.3$  the maximum lies at 1.25  $m$  (5.5.c).

For flight 4, both models admit a relatively small range of snow depths (approximately 0.2-0.25  $m$ ) with an error of 0.1 or less. The Perovich model is slightly more restrictive, producing the same estimates across all  $C$  values. The snow depth is estimated quite accurately between 0.18-0.2  $m$ , with ice thickness estimates ranging from 0.4  $m$  for isotropic scattering and 0.5  $m$  for anisotropic scattering to an upper estimate of 0.85  $m$ .

For flight 6, the estimated ranges are much larger, with snow estimates within the 0.1 error bound ranging between approximately 0.07  $m$  and 0.39  $m$  for the different values of  $C$ . The estimates assuming anisotropic scattering have larger variability, and the model suggests that the snow depth changes quite significantly with ice thickness. This is different from the models applied to the fourth run, where the snow depth estimates stay relatively consistent even as the ice thickness changes.

Comparing the modelled results with the measurements from Baffin Bay, 2016, outlined in Table 3.2, both models underestimate the possible ice thickness. During this study the transmittance was 0.023 with a mean snow thickness of 0.19  $m$  and an ice thickness of 1.28  $m$ .

Based on the studies examined in Chapter 3, snow cover on sea ice does not typically exceed 0.3  $m$ .

This means the models using the flight 6 data include results that overestimate the snow depth and underestimate the ice thickness when anisotropic scattering through ice is assumed (Figures 5.4.c 5.4.d 5.5.c 5.5.d and Figures 5.8 and 5.9).

When using the same scattering model for snow-covered and bare ice, all measurements from Table 4.4 fall well within the 0.5 error bound for the Perovich model for both runs, and about half the measurements

fall within the 0.1 boundary (Figures 5.2 and 5.4). The Nicolaus and Katlein model performs poorly on both runs, predicting almost none of the snow and ice thickness combinations within a mean relative error of 0.1 or less (Figures 5.3 and 5.5). When considering the 0.5 error boundary, the model performs adequately, with only the measurement corresponding to 0.19 *m* of snow and an ice thickness of 0.6 *m* consistently falling outside of the boundary.

Table 6.1 shows the number of data points falling within the 0.1 error bound for each model. The Perovich model applied to run 4 yields the most accurate results, followed closely by its application to run 6. The Perovich model estimates ice thickness and snow depth more accurately when isotropic scattering through snow and ice is assumed. Given that snow scattering is generally more isotropic and has a greater influence on light transmittance than ice, this likely explains the better performance, despite the more anisotropic scattering properties of sea ice.

<b>C</b>	<b>Perovich – F4</b>	<b>NK – F4</b>	<b>Perovich – F6</b>	<b>NK – F6</b>
$\pi$	8	3	8	2
2.5	8	2	7	1
1.68	8	1	6	1
1.3	8	0	4	1

Table 6.1: Number of measurements from Table 4.4 falling inside the 0.1 mean relative error boundary when estimating ice and snow thickness. Corresponding to Figures 5.2-5.5. F4 and F6 refer to flights 4 and 6, respectively. NK refers to the Nicolaus and Katlein model.

To take into account the different scattering properties of snow and ice, we re-evaluated the radiative transfer models using anisotropic scattering through bare ice and isotropic scattering through snow-covered ice, as shown in Section 5.2 Figures 5.6-5.9. We achieved the best results using the Perovich model with a scattering coefficient corresponding to  $C_i = 1.3$  for bare ice and  $C_s = \pi$  for snow-covered ice. Results were slightly improved for flight 4 versus flight 6. Figure 6.1 shows the results for run 4 with the ground truth measurements from Table 4.4 overlaid as yellow dots. The mean ice thickness (0.65 *m*) and snow depth (0.22 *m*) are marked by a white X.

While the Nicolaus and Katlein model still performs poorly, we see a significant improvement in the estimates using flight 6 data. For flight 4, the results deteriorate. The number of ground truth data points (Table 4.4) falling within the 0.1 error bound for the various parameters are shown in Table 6.2.

<b>C – Snow-Covered</b>	<b>C – Ice</b>	<b>Perovich – F4</b>	<b>NK – F4</b>	<b>Perovich – F6</b>	<b>NK – F6</b>
$\pi$	1.68	10	2	10	4
$\pi$	1.3	13	2	11	4
2.5	1.68	8	1	8	4
2.5	1.3	10	1	9	4

Table 6.2: Number of measurements from Table 4.4 falling inside the 0.1 mean relative error boundary when estimating ice and snow thickness assuming anisotropic scattering for bare ice and isotropic scattering for snow-covered ice. Corresponding to Figures 5.6 - 5.9. F4 and F6 refer to flights 4 and 6. NK refers to the Nicolaus and Katlein model.

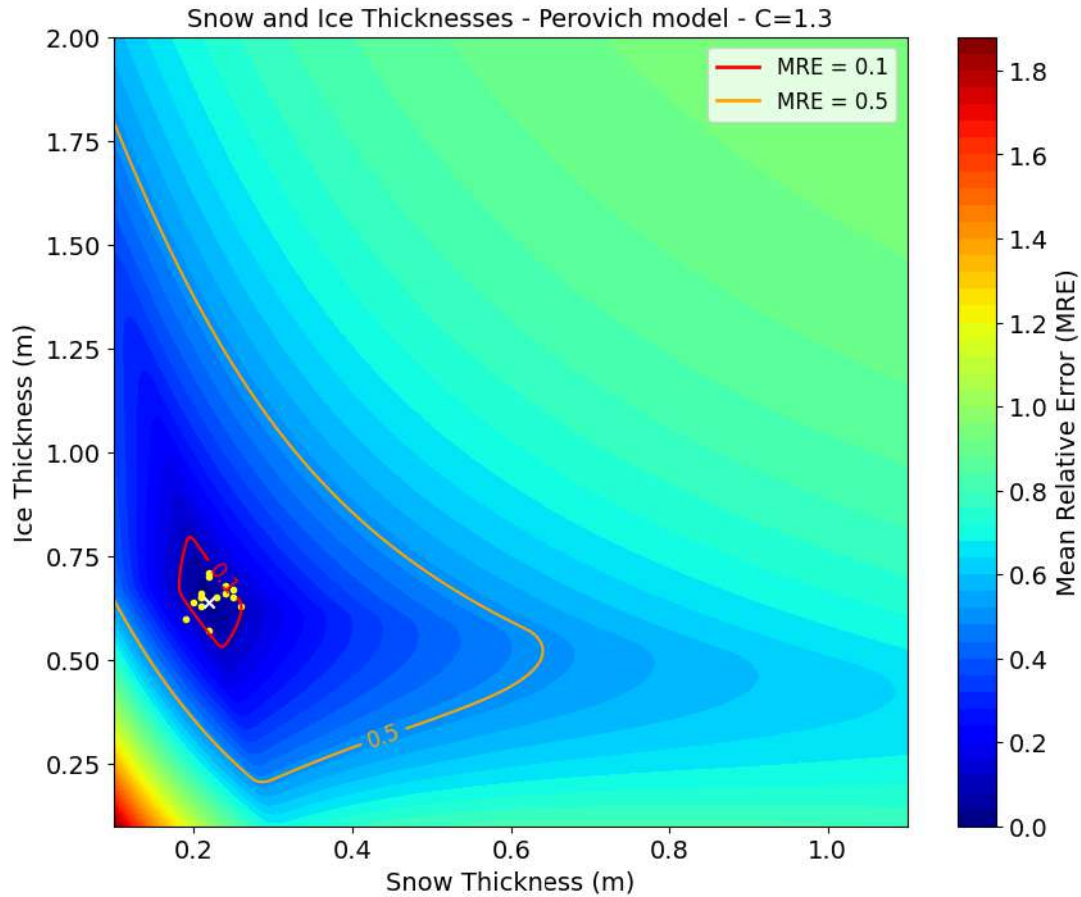


Figure 6.1: Best results of optimized snow depth and ice thickness estimations. The Perovich model is applied to data from flight 4. Scattering was assumed to be anisotropic through bare ice ( $C = 1.3$ ) and isotropic through snow-covered ice ( $C = \pi$ ). Measurements taken during field work are plotted as yellow dots, and the mean ice and snow thickness is plotted as a white X. Of the 15 ground truth snow and ice measurements (Table 4.4), 13 points are estimated within a mean relative error of less than 0.1.

### 6.3 Spectral Transmittance Results

Comparing the transmittance attained for each ice type and each flight, we see that the different  $C$  values used to convert from radiance to irradiance impact the results, and the transmittance decreases with values of  $C$ . This is logical, since the two largest  $C$  values both assume isotropic scattering through sea ice. This assumes that the light scatters evenly in all directions, and thus a significant portion of the incoming light will be scattered down through the ice. As exposed in [15], in sea ice the horizontal scattering coefficient is greater than the vertical scattering coefficient. This results in a more downward radiance distribution than predicted by isotropic models. From this we can assume that more light is scattered and absorbed before being able to pass through the entire ice sheet, and thus the overall transmittance is lower than if we assume isotropic scattering.

When comparing the calculated spectral transmittance between flights 4 and 6, the first thing to notice is the discrepancy in shape (see Figure 5.11). The transmittance calculated for run 4 is surprisingly low in the blue wavelengths (450-495  $nm$ ), at only 25-35% of the transmittance in the green wavelengths (495-570  $nm$ ). For the bare ice, the transmittance in the blue wavelengths is even lower than the transmittance in the red wavelengths (620-750  $nm$ ). When comparing these results to those in Figure 3.3 [22], the spectral shape matches most closely to that of the first-year melting snow-covered ice with

a high concentration of algae. However, since our measurements were taken early in the spring we do not expect such an algae layer to be present, and therefore would not expect this spectral shape. Furthermore, measurements were taken in cold temperatures around  $-25^{\circ}\text{C}$ , before melt onset. The spectral transmittance calculated from run 6 data is much closer to what we expect, and the bare ice transmittance matches the spectral shape of the first-year bare ice transmittance in Figure 3.3. The only difference here is that our calculated transmittance is significantly higher, even for the lowest  $C$  value. This can be explained by the fact that our measurements were taken through ice with an average thickness of  $0.65\text{ m}$ , while the measurements presented in Figure 3.3 were taken through  $1.4\text{ mm}$  thick ice, and transmittance decreases roughly exponentially with increasing ice thickness [22].

Table 5.2 allows us to easily see how much of the overall incoming visible light reaches the bottom of the ice. For flight 4 the transmittance through snow-covered ice is approximately 4-5% of the transmittance through bare ice. For flight 6 this is slightly higher, between 8-12%. The overall transmittance through bare ice decreases by about 30% between the afternoon and evening, while it stays relatively constant through snow-covered ice, with even a slight apparent increase in transmittance. The decrease in transmittance through bare ice can be explained by the change in sun angle, with the lower angle causing more light to be reflected off the surface. Further, due to the lower angle of incidence, the incoming light has a longer path to travel to reach the bottom of the ice, and more scattering can occur, further decreasing the amount of light that is transmitted.

The scattering in snow is much more isotropic than in sea ice. This means that much of the light gets scattered in all directions in the snow layer, and so the incoming sunlight angle has less of an impact on transmittance. Additionally, snow is highly absorbent. This explains the relatively stable transmittance values through the snow-covered ice.

The relative behaviour of transmittance through bare and snow-covered sea ice is consistent with state of the art radiative transfer physics. Comparing with results in Table 3.2, total transmittance through snow-covered ice ranges from 0.0019 (row 7) to 0.041 (row 8). The study most closely coinciding with our measured snow depth and ice thickness is that from Storfjorden on Svalbard in 2016 (row 3), where a total transmittance of 0.003 was measured, which is one order of magnitude lower than our results. The transmittance values most closely matching our results are from Baffin Bay, 2016 (row 2). Here, there was a much higher ice thickness, but a snow thickness similar to our measurements, and a transmittance of 0.023.

The only bare ice transmittance measurement in Table 3.2 comes from an ice thickness almost twice of what we had, and a transmittance ranging from 0.03-0.22. The upper limit of this range matches our calculated transmittance when we assume anisotropic scattering. We expect our results to be higher overall, since transmittance decreases with ice thickness.

The transmittance measured during the MOSAiC project cannot be directly compared with our results, since the measurements were taken in July, with a large concentration of melt ponds, and much thicker ice ( $2.7\text{ m}$ ).

## 6.4 Limitations

While we have achieved promising results estimating ice thickness using under-ice light transmittance, we need to consider several limitations of our approach.

The method relies on collecting under-ice light transmittance data, which necessitates deploying an ROV or similar instrument. This process is both time-consuming and costly, compounded by extreme polar temperatures and remote locations. Although the UHI is designed for air temperatures between  $-5^{\circ}\text{C}$  to  $+25^{\circ}\text{C}$ , we operated in significantly colder conditions, as many polar excursions in the spring would.

Consequently, our data are limited to a single field excursion to Van Mijenfjorden, meaning all of our analyses are based on snow and ice conditions specific to that environment. As such, we cannot say how well these findings generalize to other conditions, such as varying snow and ice thicknesses, different ice types (*e.g.* deformed, ridged, or nilas), fresh versus old snow, differing brine concentrations, or varying levels of impurities within the ice. Replicating the experiments under a broader range of conditions would be beneficial to assess the robustness of our findings.

However, we were able to capture data under different incoming light conditions, with measurements taken near noon and just before sunset. Achieving comparable results with these data is encouraging.

A practical challenge encountered during the data processing was the manual identification of snow-covered versus bare sections of the ice in the RGB images generated by the DBE. This process is time-consuming and limits the development of fully modular code for the analysis.

To ensure the feasibility of our analysis, assumptions and simplifications were made concerning the physical and optical properties of snow and ice. Lacking a spectroradiometer during fieldwork, we modelled albedo based on known physical snow properties, rather than directly measuring it. We neglect the effects of brine volume, mineral content, and dust impurities to simplify the analysis. Since the data were collected early in the season, no under-ice algae layer was present. However, if we were to apply this method in later spring, the significant light absorption by algae, as documented in previous research (see Chapter 3), would need to be taken into account.

The surface scattering layer also significantly impacts the inherent optical properties of snow and ice ([11, 12]), influencing light transmittance. Recent research by Katelin, Nicolaus, and Petrich [15] indicates that sea ice scattering is predominantly anisotropic. Accurate calculations of transmitted irradiance depend on knowledge of the anisotropic scattering coefficient. Since we did not have these data, we conducted our analysis using four different anisotropic scattering coefficients to capture a range of possible conditions.

We further simplified the analysis by ignoring the effect of the water column on light transmittance. While this factor has been addressed in recent work [54], it was beyond the scope of our study.

# Chapter 7

## Conclusion

The primary goal of this thesis was to develop a non-invasive method to estimate sea ice thickness using under-ice light transmittance data. In this process, we explored the relationship between light transmittance, the physical and optical properties of snow and ice, and ice thickness. Radiance data were successfully collected in the challenging Arctic conditions in Van Mijenfjorden, Svalbard, using a DBE robotic platform equipped with a UHI camera. We completed several under-ice flights, overcoming navigational and operational challenges. Our analysis of spectral attenuation through ice and snow from runs 4 and 6 provided detailed measurements of spectral irradiance and transmittance. Applying the radiative transfer models presented by Perovich [11] and by Nicolaus and Katlein [24], we calculated spectral extinction coefficients and estimated ice thickness. The retrieved extinction coefficients were consistent with previous studies. The Perovich model, applied to flight 4 with the assumptions of anisotropic scattering through bare ice and isotropic scattering through snow-covered ice, achieved the most accurate ice thickness estimates. This supports the findings by Katlein, Nicolaus, and Petrich [15], who suggest that scattering through sea ice is predominantly anisotropic. The Nicolaus and Katlein model performed poorly in comparison to ground truth measurements.

Using under-ice light transmittance to measure thickness presents a valuable, minimally invasive alternative to traditional methods such as ice coring, as the approach reduces environmental impact and requires less manual labour. It also yields a more comprehensive view of overall ice thickness and snow depth than can be achieved with under-ice sonars, which typically only provide ice draft measurements. The distinct optical properties of snow and ice make it possible to discern between ice and snow layers, enabling estimations of snow depth in addition to ice thickness. The approach is scalable and can be applied over large areas and extended periods of time, offering potential improvements in climate modelling, Arctic ecosystem management, and marine and maritime operations in polar regions.

The collected data contribute to the still limited body of Arctic research and can also support further research in related fields. Specifically, the additional information on under-ice light transmittance acquired through this study can aid with the understanding of biological processes and ecosystem studies that rely on light availability and intensity. In optical modelling, the dataset and our achieved results can be used to test and improve other radiative transfer models. The dataset can also be used as a benchmark for long-term monitoring of the sea-ice melting rate and snow trends in the Arctic, as the climate continues to change.

The research presented in this thesis could be extended by replicating the experiments under varying environmental conditions, including different snow and ice thicknesses. More repetitions of the experi-

ment would also improve the accuracy of the results. Future work should incorporate measured albedo values and the anisotropic scattering coefficient of the ice. Applying more advanced radiative transfer modelling techniques that account for brine volume, ice and snow impurities, and the influence of the water column on light transmission, would further refine the results.

Exploring the use of under-ice buoys and integrating this method with satellite remote sensing could also open new possibilities for long-term and large-scale sea ice thickness monitoring.

In conclusion, our results show a significant correlation between ice thickness, snow depth, and light transmittance. The detailed spectral resolution provided by the UHI makes it possible to identify the optical properties of snow and ice, leading to accurate sea ice thickness estimations. This validates the feasibility of using UHI data in this capacity. We have successfully demonstrated the potential of this novel approach, which holds significant implications for both scientific research and practical applications in polar regions. As Arctic sea ice continues to decline, developing innovative, scalable methods for monitoring ice thickness is essential for advancing our understanding of Arctic environments and their role in the global climate system.

# Bibliography

- [1] M. Nicolaus, D. K. Perovich, G. Spreen, M. A. Granskog, L. von Albedyll, M. Angelopoulos, P. Anhaus, S. Arndt, H. J. Belter, V. Bessonov, G. Birnbaum, J. Brauchle, R. Calmer, E. Cardellach, B. Cheng, D. Clemens-Sewall, R. Dadic, E. Damm, G. de Boer, O. Demir, K. Dethloff, D. V. Divine, A. A. Fong, S. Fons, M. M. Frey, N. Fuchs, C. Gabarró, S. Gerland, H. F. Goessling, R. Gradinger, J. Haapala, C. Haas, J. Hamilton, H.-R. Hannula, S. Hendricks, A. Herber, C. Heuzé, M. Hoppmann, K. V. Høyland, M. Huntemann, J. K. Hutchings, B. Hwang, P. Itkin, H.-W. Jacobi, M. Jaggi, A. Jutila, L. Kaleschke, C. Katlein, N. Kolabutin, D. Krampe, S. S. Kristensen, T. Krumpfen, N. Kurtz, A. Lampert, B. A. Lange, R. Lei, B. Light, F. Linhardt, G. E. Liston, B. Loose, A. R. Macfarlane, M. Mahmud, I. O. Matero, S. Maus, A. Morgenstern, R. Naderpour, V. Nandan, A. Niubom, M. Oggier, N. Oppelt, F. Pätzold, C. Perron, T. Petrovsky, R. Pirazzini, C. Polashenski, B. Rabe, I. A. Raphael, J. Regnery, M. Rex, R. Ricker, K. Riemann-Campe, A. Rinke, J. Rohde, E. Salganik, R. K. Scharien, M. Schiller, M. Schneebeli, M. Semmling, E. Shimanchuk, M. D. Shupe, M. M. Smith, V. Smolyanitsky, V. Sokolov, T. Stanton, J. Stroeve, L. Thielke, A. Timofeeva, R. T. Tonboe, A. Tavri, M. Tsamados, D. N. Wagner, D. Watkins, M. Webster, and M. Wendisch, "Overview of the MOSAiC expedition: Snow and sea ice," *Elementa: Science of the Anthropocene*, vol. 10, p. 000046, 02 2022.
- [2] W. Weeks, *On Sea Ice*. University of Alaska Press, 2010.
- [3] H. Sumata, L. de Steur, D. V. Divine, M. A. Granskog, and S. Gerland, "Regime shift in arctic ocean sea ice thickness," *Nature*, vol. 615, pp. 443–449, 2023.
- [4] A. J. Cook, J. Dawson, S. E. L. Howell, J. E. Holloway, and M. Brady, "Sea ice choke points reduce the length of the shipping season in the northwest passage," *Communications Earth and Environment*, vol. 5, no. 362, 2024.
- [5] R. Shamshiri, E. Eide, and K. V. Høyland, "Spatio-temporal distribution of sea-ice thickness using a machine learning approach with Google Earth Engine and Sentinel-1 GRD data," in *Remote Sensing of Environment*, 2022.
- [6] G. Timco and W. Weeks, "A review of the engineering properties of sea ice," *Cold Regions Science and Technology*, vol. 60, no. 2, pp. 107–129, 2010.
- [7] M. Nicolaus, C. Katlein, J. Maslanik, and S. Hendricks, "Changes in arctic sea ice result in increasing light transmittance and absorption," *Geophysical Research Letters*, vol. 39, no. 24, 2012.
- [8] N. Summers, *Identification, mapping, and photobiology of Arctic macro- and microalgae using ROV-UHI*. PhD thesis, Norwegian University of Science and Technology, 2024.

- [9] V. Coppolaro, “Sea ice underside three-dimensional topography and draft measurements with an upward-looking multibeam sonar mounted on a remotely operated vehicle,” Master’s thesis, Università Degli Studi Firenze, 2018.
- [10] S. Sandven, R. K. Hansen, E. Eknes, B. Kvingedal, K. Bruserud, F. Nilsen, J. Wåhlin, H. Sagen, and K. Kloster, “ICESONAR Monitoring of sea ice thickness from a subsea 4D Sonar,” tech. rep., Nansen Environmental and Remote Sensing Center, 2010.
- [11] D. Perovich, *The Optical Properties of Sea Ice*. U.S. Army Cold Regions Research and Engineering Laboratory, 1996.
- [12] B. Light, D. K. Perovich, M. A. Webster, C. Polashenski, and R. Dadic, “Optical properties of melting first-year arctic sea ice,” *Journal of Geophysical Research: Oceans*, vol. 120, p. 7657–7675, 2015.
- [13] D. Perovich and T. Grenfell, “Laboratory studies of the optical properties of young sea ice,” *Journal of Glaciology*, vol. 27, pp. 331–346, 1981.
- [14] S. G. Warren, “Optical properties of ice and snow,” *Philosophical transactions. Series A, Mathematical, physical, and engineering sciences*, vol. 377, no. 2146, 2019.
- [15] C. Katlein, M. Nicolaus, and C. Petrich, “The anisotropic scattering coefficient of sea ice,” *Journal of Geophysical Research: Oceans*, vol. 119, pp. 842–855, 2014.
- [16] P. Anhaus, C. Katlein, M. Nicolaus, S. Arndt, A. Jutila, and C. Haas, “Snow depth retrieval on arctic sea ice using under-ice hyperspectral radiation measurements,” *Frontiers in Earth Science*, 2021.
- [17] C. Katlein, S. Arndt, M. Nicolaus, D. K. Perovich, M. V. Jakuba, S. Suman, S. Elliott, L. L. Whitcomb, C. J. McFarland, R. Gerdes, A. Boetius, and C. R. German, “Influence of ice thickness and surface properties on light transmission through Arctic sea ice,” *Journal of Geophysical Research: Oceans*, vol. 120, no. 9, pp. 5932–5944, 2015.
- [18] K. Høyland, *Arctic Marine Measurements Techniques, Operations and Transport AT-334/834 - Module 1 Sea ice and Icebergs*. The Norwegian University of Science and Technology (NTNU), The University Centre in Svalbard (UNIS), 2023.
- [19] S. Gerland and R. Hall, “Variability of fast-ice thickness in Spitsbergen fjords,” *Annals of Glaciology*, vol. 44, p. 231–239, 2006.
- [20] G. A. Maykut and N. Untersteiner, “Some results from a time-dependent thermodynamic model of sea ice,” *Journal of Geophysical Research (1896-1977)*, vol. 76, no. 6, pp. 1550–1575, 1971.
- [21] S. Løset, K. Shkhinek, and K. Høyland, *Ice Physics and Mechanics*. The Norwegian University of Science and Technology (NTNU), 1998.
- [22] D. Perovich, *Sea Ice: Third Edition*, ch. Sea ice and sunlight. Cold Regions Research and Engineering Laboratory, Hanover, NH, USA, 2016.
- [23] M. Nicolaus, C. Petrich, S. R. Hudson, and M. A. Granskog, “Variability of light transmission through arctic land-fast sea ice during spring,” *The Cryosphere*, no. 3, p. 977–986, 2013.
- [24] M. Nicolaus and C. Katlein, “Mapping radiation transfer through sea ice using a remotely operated vehicle (rov),” *The Cryosphere*, no. 3, pp. 763–777, 2013.

- [25] NASA, “NASA’s ICESat-2 Measures Arctic Ocean’s Sea Ice Thickness, Snow Cover.” <https://www.nasa.gov/centers-and-facilities/goddard/nasas-icesat-2-measures-arctic-oceans-sea-ice-thickness-snow-cover>, 2020. [Online; accessed 16-Apr-2024].
- [26] E. Cimoli, K. Meiners, A. Lucieer, and V. Lucieer, “An under-ice hyperspectral and rgb imaging system to capture fine-scale biophysical properties of sea ice,” *Remote Sens.* *11*, 2860, 2019.
- [27] Z. Junbao, L. Shuo, and L. Ya, “Application of unmanned underwater vehicles in polar research,” *Advances in Polar Science*, vol. 32(3), p. 173–184, 2021.
- [28] G. D. Williams, A. Fraser, A. Lucieer, D. Turner, E. Cougnon, P. Kimball, T. Maksym, H. Singh, T. Toyota, and M. Paget, “Drones in a cold climate,” *EOS Transactions*, 2016.
- [29] A. A. Mogstad, “A practical guide to spectrometer analysis and underwater hyperspectral imaging.” NTNU AMOS, Department of Biology, 2020.
- [30] J. Qin, “Hyperspectral imaging instruments,” *Hyperspectral Imaging for Food Quality Analysis and Control*, 12 2010.
- [31] J. M. Amigo, *Hyperspectral imaging*. Elsevier, 2019.
- [32] G. Johnsen, Z. Volent, H. Dierssen, R. Pettersen, M. Ardelan, F. Søreide, P. Fearn, M. Ludvigsen, and M. Moline, *Subsea Optics and Imaging*, ch. 508-535. Woodhead Publishing: Sawston, UK, 2013.
- [33] B. Liu, Z. Liu, S. Men, Y. Li, Z. Ding, J. He, and Z. Zhao, “Underwater Hyperspectral Imaging Technology and Its Applications for Detecting and Mapping the Seafloor: A Review,” *Sensors*, vol. 20, no. 17, 2020.
- [34] M. Ferrera, A. Arnaubec, K. Istenic, N. Gracias, and T. Bajjouk, “Hyperspectral 3d mapping of underwater environments,” in *in 2021 IEEE/CVF International Conference on Computer Vision Workshops (ICCVW)*, 2021.
- [35] A. A. Mogstad, G. Johnsen, and M. Ludvigsen, “Shallow-water habitat mapping using underwater hyperspectral imaging from an unmanned surface vehicle: A pilot study,” in *Remote Sensing*, vol. *11*, no. 6, 2019.
- [36] Ødegård, A. A. Mogstad, G. Johnsen, A. J. Sørensen, and M. Ludvigsen, “Underwater hyperspectral imaging: a new tool for marine archaeology,” *Applied Optics*, vol. 57, no. 12, p. 3214, 2018.
- [37] J. C. Montes-Herrera, E. Cimoli, V. Cummings, N. Hill, A. Lucieer, and V. Lucieer, “Underwater Hyperspectral Imaging (UHI): A Review of Systems and Applications for Proximal Seafloor Ecosystem Studies,” *Remote Sensing*, vol. 13, no. 17, 2021.
- [38] H. S. Løvås, A. J. Sørensen, and M. Ludvigsen, “Framework for combining multiple lightweight underwater vehicles into super underwater vehicle,” in *2020 IEEE/OES Autonomous Underwater Vehicles Symposium (AUV)*, pp. 1–6, 2020.
- [39] A. Chennu, P. Faerber, G. De’ath, D. de Beer, and K. Fabricius, “A diver-operated hyperspectral imaging and topographic surveying system for automated mapping of benthic habitats,” *Sci. Rep.*, *7*, 7122, 2017.
- [40] E. AS, “Uhi calibration and test certificate.” Trondheim, Norway.

- [41] M. Lebrun, M. Vancoppenolle, G. Madec, M. Babin, G. Becu, A. Lourenço<sup>1</sup>, D. Nomura, F. Vivierl, and B. Delille, "Light under arctic sea ice in observations and earth system models," *Journal of Geophysical Research: Oceans*, vol. 128, no. 3, 2023.
- [42] B. Light, T. C. Grenfell, and D. K. Perovich, "Transmission and absorption of solar radiation by arctic sea ice during the melt season," *Journal of Geophysical Research: Oceans*, vol. 113, 2008.
- [43] C. J. Mundy, J. K. Ehn, D. G. Barber, and C. Michel, "Influence of snow cover and algae on the spectral dependence of transmitted irradiance through arctic landfast first-year sea ice," *Journal of Geophysical Research: Oceans*, vol. 112, no. C3, 2007.
- [44] P. Wongpan, D. Nomura, T. Toyota, T. Tanikawa, K. M. Meiners, T. Ishino, T. P. Tamura, M. Tozawa, Y. Nosaka, T. Hirawake, and et al., "Using under-ice hyperspectral transmittance to determine landfast sea-ice algal biomass in saroma-ko lagoon, hokkaido, japan," *Annals of Glaciology*, vol. 61, no. 83, p. 454–463, 2020.
- [45] T. Grenfell and G. Maykut, "The optical properties of ice and snow in the arctic basin," *Journal of Glaciology*, vol. 18, pp. 445–463, 1977.
- [46] N. Summers, G. Johnsen, A. Mogstad, H. Løvås, G. Fragoso, and J. Berge, "Underwater Hyperspectral Imaging of Arctic Macroalgal Habitats during the Polar Night Using a Novel Mini-ROV-UHI Portable System," *Remote Sensing*, vol. 14, no. 6, 2022.
- [47] J. Schanda, *Colorimetry: understanding the CIE system*. John Wiley 'l&' Sons, 2007.
- [48] NOAA Global Monitoring Laboratory, "Noaa solar calculator." <https://gml.noaa.gov/grad/solcalc/>, 2023. Accessed: 2024-06-15.
- [49] G. Johnsen, K. M. Kovacs, and E. Sakshaug, *Ecosystem Barents Sea*, ch. 5. Tapir Academic Press, Trondheim. Norway, 2009.
- [50] Q. Libois, G. Picard, J. France, L. Arnaud, M. Dumont, C. Carmagnola, and M. King, "Influence of grain shape on light penetration in snow," *The Cryosphere*, vol. 7, no. 6, pp. 1803–1818, 2013.
- [51] N. K. S. Senter, "Historical air temperature data," 2024. Accessed: 2024-04-03.
- [52] A. R. Macfarlane, H. Löwe, L. Gimenes, D. N. Wagner, R. Dadic, R. Ottersberg, S. Hämmerle, and M. Schneebeli, "Temporospatial variability of snow's thermal conductivity on arctic sea ice," *The Cryosphere*, vol. 17, no. 12, p. 5417–5434, 2023.
- [53] P. Schwerdtfeger, "The thermal properties of sea ice," *Journal of Glaciology*, vol. 4, no. 36, p. 789–807, 1963.
- [54] H. Liu, N. Summers, Y.-C. Chen, H. S. Løvås, G. Johnsen, D. Koestner, C. Sætre, and S. Hamre, "Pixelwise immersion factor calibration for underwater hyperspectral imaging instruments," *Optics Express*, no. 11, pp. 19854–19880, 2024.